TAMPEREEN TEKNILLINEN YLIOPISTO
TAMPERE UNIVERSITY OF TECHNOLOGY
Julkaisu 557 • Publication 557

Antti Happonen

Decomposition of Radon Projections into Stackgrams for Filtering, Extrapolation, and Alignment of Sinogram Data

Tampere 2005

Tampereen teknillinen yliopisto. Julkaisu 557
Tampere University of Technology. Publication 557

Antti Happonen

Decomposition of Radon Projections into Stackgrams for Filtering, Extrapolation, and Alignment of Sinogram Data

Thesis for the degree of Doctor of Technology to be presented with due permission for public examination and criticism in Tietotalo Building, Auditorium TB109, at Tampere University of Technology, on the 18th of November 2005, at 12 noon.

Tampereen teknillinen yliopisto - Tampere University of Technology
Tampere 2005

ISBN 952-15-1465-5 (printed)
ISBN 952-15-1496-5 (PDF)
ISSN 1459-2045

Abstract

In computed tomography, information about inner structures of an object (or a patient) is obtained indirectly by numerically reconstructing an image of the object from its measured projections. The measured Radon projections are represented as a sinogram matrix, which can be regarded as a digital image. The sinogram image consists of different mixed and summed sinusoidal curves. Signals along these sinusoids or trajectories contribute to pixel values of the reconstructed image. The reconstructed image can represent, for example, the tracer distribution in the body as in positron emission tomography (PET).

Due to the low signal–to–noise ratio in measured sinograms in emission tomography, starting point for the thesis has been to develop a procedure to improve the reconstructed image quality from a novel point of view. In the thesis, we present a novel decomposition for the signals along the sinusoidal trajectories of the sinogram. This decomposition, or the "stackgram" approach, allows processing separately the sinusoidal trajectory signals. In the stackgram representation, the signals can be processed without interfering with the crossing trajectories. This new stackgram approach can be regarded as an intermediate form of the sinogram and reconstructed image representations. A mathematical transformation from the sinogram data into the stackgrams is simple and invertible, and has been introduced in the thesis. In addition, the new stackgram approach is employed for three different applications of the sinogram data.

A proper noise reduction is a relevant issue especially in emission tomography; therefore the first discussed application is data filtering employing the stackgram representation for noise reduction of the sinograms. According to our experimental studies, filtering of the stackgram data does not introduce geometrical distortions in the reconstructed images, and the noise structure of the images is visually not disturbing. These suggest that the stackgram filtering approach can provide a potential alternative to a common sinogram filtering procedure (denoted as radial filtering).

In addition to filtering, we have successfully employed the stackgrams for extrapolation of incomplete sinogram data for limited angle tomography in the thesis. In limited angle tomography the full range of projection views is not

available as in the normal case, but it can be numerically estimated for image reconstruction.

The third application presented in the thesis is alignment of the tomographic data. Motion of the object or the patient as well as motion of the organs during the scan cause blurring and artifacts in the reconstructed images. To avoid the artifacts, the scans can be divided into short time frames. The different frames are then numerically aligned for a reference frame, in order to compensate the motion. For the task like this, the proposed stackgram based data–driven alignment algorithm is fully automatic, simple, and it is suited for alignment of the data having small changes in spatial positions or structures. This kind of an automated data–driven alignment technique for the sinogram data is desired especially in modern emission tomographs.

Preface

This work was carried out at the Institute of Signal Processing, Tampere University of Technology, during the years 2002-2005. The idea of the work was already born in the year 2000 after my summer trainee period at the institute.

I thank my both supervisors Docent Ulla Ruotsalainen and PhD Sakari Alenius for their advice and guidance. I am grateful to Docent Ruotsalainen for her invaluable supervision and encouragement. I am also indebted to Docent Ruotsalainen for organizing the funding for the work, which made the thesis possible. I am deeply indebted to PhD Alenius for his guidance and support especially in the starting time of the work. PhD Alenius gave a significant contribution to the birth of this work.

The reviewers of this thesis, Professor Brian F. Hutton (University College London) and Professor Jari P. Kaipio (University of Kuopio), deserve sincere thanks for their careful reading of the manuscript, and detailed feedback.

I want to express my gratitude to my colleagues in our research group, M^2oBSI, for their support. I also thank my fellow workers at the Institute of Signal Processing. It has been pleasure to share such a relaxed and international working environment.

This work was financially supported by the Academy of Finland (projects 73238 and 104834), TEKES (Drug2000 Technology Program), the Finnish Society for Promotion of Technology grant (TES), and the Finnish Foundation for Economics and Technology Sciences grant (KAUTE). I gratefully acknowledge the organizations for their support.

Antti Happonen
Tampere, the 1st of November 2005

Supervisors: Docent Ulla Ruotsalainen
Institute of Signal Processing
Tampere University of Technology

PhD Sakari Alenius
Nokia Research Center, Tampere

Reviewers: Professor Brian F. Hutton
Institute of Nuclear Medicine
University College London

Professor Jari P. Kaipio
Department of Applied Physics
University of Kuopio

Opponents: Professor Brian F. Hutton
Institute of Nuclear Medicine
University College London

Professor Johan Nuyts
Division of Nuclear Medicine
Katholieke Universiteit Leuven

Tampere University of Technology
Department of Information Technology
Institute of Signal Processing
Methods and Models for Biological Signals and Images (M^2oBSI) Group

Contents

List of Publications

This thesis is based on the following publications. These are referred in the text as [P-$*$], where $*$ denotes a corresponding number to the publication as follows.

Publication-1 A. P. Happonen and S. Alenius, "Sinogram Filtering Using a Stackgram Domain", *Proceedings of the Second IASTED International Conference: Visualization, Imaging and Image Processing*, Malaga, Spain, September 9-12, 2002, pp. 339-343

Publication-2 A. P. Happonen and S. Alenius, "Investigation of Sinogram Filtering Using Stackgram Domain", *IEEE Transactions on Medical Imaging*, (submitted, February 2003)
Published as a technical report of Tampere University of Technology, Institute of Signal Processing, *Report 2005:1*, October 2005

Publication-3 A. P. Happonen and S. Alenius, "A Comparison of Sinogram and Stackgram Domain Filtering Methods Employing L-Filters for Noise Reduction of Tomographic Data", *Proceedings of the 2005 Finnish Signal Processing Symposium*, Kuopio, Finland, August 25, 2005, pp. 1-4

Publication-4 A. P. Happonen and U. Ruotsalainen, "A Comparative Study of Angular Extrapolation in Sinogram and Stackgram Domains for Limited Angle Tomography", *14th Scandinavian Conference SCIA 2005, Lecture Notes in Computer Science*, Vol. 3540, June 2005, pp. 1047-1056

Publication-5 A. P . Happonen and U. Ruotsalainen, "Three-Dimensional Alignment of Scans in a Dynamic PET Study Using Sinusoidal Trajectory Signals of a Sinogram", *IEEE Transactions on Nuclear Science*, Vol. 51, No. 5, October 2004, pp. 2620-2627

List of abbreviations

ART	Algebraic reconstruction technique
CBP	Convolution back–projection
CPL	Clark–Palmer–Lawrence interpolation
FBP	Filtered back–projection
FIR	Finite impulse response
FOV	Field of view
FWHM	Full–width–at–half–maximum
GP	Gerchberg–Papoulis extrapolation
MAE	Mean absolute error
MAF	Multiple acquisition frame
MAP	Maximum–a–posteriori
MLEM	Maximum likelihood - expectation maximization
MRP	Median root prior
MSE	Mean square error
NEC	Noise equivalent count
PET	Positron emission tomography
POCS	Projections onto convex sets

Chapter 1

Introduction

Reconstruction of a cross–section of an object from its transaxial projections is an important problem in image processing. This kind of problem refers to tomography. In computed tomography, information about inner structures of the measured object is obtained indirectly by reconstructing an image of the object from its one dimensional projections or line integrals [24]. Image reconstruction from projections is generally modeled by the inversion of the Radon transform, introduced already in 1917 by Johann Radon. The inversion is a moderately ill–posed problem, making the image reconstruction challenging in practice due to noise.

The transaxial projections of a cross–section of the measured object are represented as a sinogram matrix, where the horizontal row refers to radial samples and the vertical column refers to evenly spaced angular views (see the geometry in Fig. 1.1). In practice, noise in the measured projections deteriorates the quality of the reconstructed images. This is a problem especially in positron emission tomography (PET) [55]. Generally accepted methods to reduce the noise in the sinogram data are radial filtering (filtering along the rows of the sinogram) and axial filtering in the case of three dimensional data (the sinograms are filtered across the individual cross-sections of a three dimensional image). In contrast, filtering of the sinograms along the angular direction (across the sinogram rows) is commonly avoided, since it introduces observable non–uniform blurring in reconstructed images [13]. In addition, many different reconstruction methods that reduce the noise have been introduced, such as the iterative median root prior (MRP) algorithm [1], to improve the PET–image quality.

In order to reconstruct an image from the sinogram data, evenly spaced projections are required within the interval $[0^\circ\ 180^\circ)$. However, in limited angle tomography [45] this full range of projection views is not available, but some angular views are missing. With standard image reconstruction algorithms, this

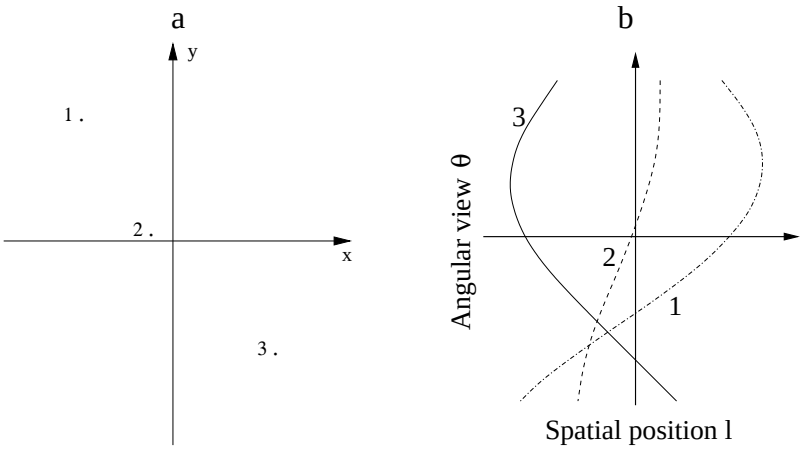

Figure 1.1: An illustration of the image and sinogram domains: a) three points in the image domain; b) the corresponding trajectory signals in the sinogram domain.

results in artifacts in reconstructed images, if the missing data values are not compensated. A method to compensate for the lack of the angular views is to extrapolate the sinogram matrix along the angular direction. This, however, can introduce tangential blurring similarly as in the case of angular sinogram filtering, since extrapolation can be regarded as a signal filtering application. Reconstruction algorithms for the limited angle data have been presented as well (see e.g. [56]). These algorithms compensate the incomplete sinogram data during the reconstruction process, instead of direct extrapolation in the sinogram domain.

In practice, a patient is being scanned with a tomograph in order to get the cross–sectional images from the measured sinograms. Regardless of the imaging modality, the patient and organ motions during the acquisition cause blurring and artifacts to the reconstructed images, besides the noise. Many different registration algorithms have been presented to solve this kind of problem to avoid the artifacts caused by motion (see e.g. reviews [82, 49, 25]). Most of the proposed algorithms employ the reconstructed images, instead of the sinogram data, for the registration, since then the movement detection and the registration are more straightforward in practice.

In this thesis, we present a new stackgram[1] approach [P-1] for processing of the tomographic data. The stackgram representation decomposes the signals along the sinusoidal trajectories of the sinogram (see Fig. 1.1). Therefore the

[1]The word “stackgram” can be pronounced as it would be written as “stackogram”

signals along these trajectories can be processed separately or without affecting the other crossing trajectory signals. The stackgram domain, to be defined, can be seen as an intermediate form of the image and sinogram representations. The sinogram data are duplicated and reorganized in the stackgrams, and thus the stackgram data have more sinogram than image like properties. Motivation of the thesis is that the stackgram approach can allow processing of the sinogram data using the angular information in a more convenient manner.

In this thesis, we concentrate on a deterministic approach[2] in three different applications of the stackgrams. First, the stackgrams are applied for filtering of noisy sinograms. Furthermore, the stackgram domain is utilized for extrapolation of the missing data for limited angle tomography. Finally, the stackgram approach is employed for alignment of object movements between short time frames resulting in motion compensated sinograms, or alternatively "stackgram–reconstructed" images. To be emphasized, none of these three proposed applications of the stackgram domain requires image reconstruction (prior to processing of the stackgrams), and thereby artifacts introduced by the ill–posed reconstruction process are not affected.

In Chapter 2, image reconstruction from projections is reviewed and related issues are considered in continuous case. Chapter 3 considers representations of the projections as well as image reconstruction in discrete case. The stackgram domain and its properties are described in Chapter 4. We review sinogram filtering, limited angle tomography, and image registration in Chapters 5, 6, and 7, respectively. Chapter 8 summarizes the methods and results of the thesis for the above three applications. In Chapter 9, the known problems and advantages of the stackgram domain approach are discussed.

[2] Another approach for the problem would be provided by the statistical inversion paradigm, in which both the measurement errors and the unknown variables are treated as random variables [31].

Chapter 2

Principles of Image Reconstruction from Projections

Integrations along straight lines through the object are referred as line integrals. Projections are denoted as a set of the line integrals of the unknown function with a parameter of the object being measured [32]. Examples of the measurement like this are the X–ray absorption of the tissue, and the number of emitted photons in positron emission tomography. This chapter starts with the definition of the line integrals and the Radon transform[1] that give the basis for the modeling of image reconstruction from projections. In this chapter we also briefly discuss the Radon transform related mappings in continuous case, before introducing the projection theorem. For simplicity through the thesis, we consider only definitions and algorithms based on parallel beam projection data. Most of the definitions are presented only in two dimensional cases, although some of the definitions could be formulated on the n dimensional case.

2.1 The Radon Transform

An integral of some parameter over the object along a line is denoted as a line integral. A line through (x, y) position at the angle θ can be written in the two dimensional case as

$$l = x\cos\theta + y\sin\theta. \tag{2.1}$$

The line integral or the Radon projection $p_\theta(l)$ can be defined thereby as [32]

$$p_\theta(l) = \int_{(\theta,l)\ line} f(x,y)ds. \tag{2.2}$$

[1] In seismology, the Radon transform is known as the tau-P transform or the slant stack [7].

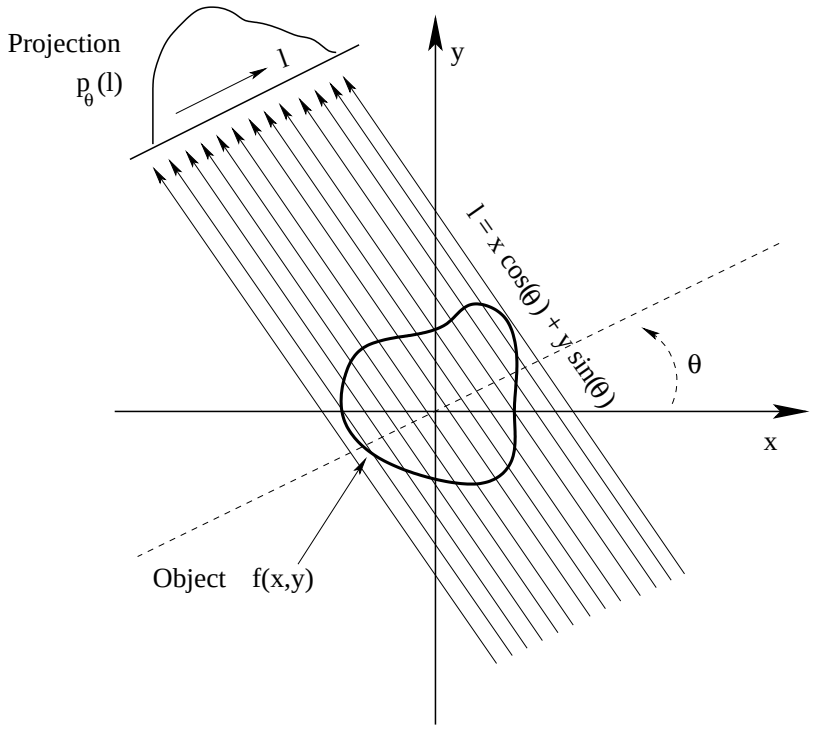

Figure 2.1: A function $f(x, y)$ and one of its projections $p_\theta(l)$ at the angle θ. The projection is a set of integrals along the parallel lines. The function $g(l, \theta)$ is a collection of the projections $p_\theta(l)$ for a number of different angles.

Using the above relationships, the Radon transform $g(l, \theta)$ of a function $f(x, y) \in \mathbb{R}^2$ can be defined with a delta function as [29, 53]

$$g(l, \theta) \triangleq \mathcal{R}f = \int \int_{-\infty}^{\infty} f(x, y)\delta(x \cos\theta + y \sin\theta - l)dxdy. \tag{2.3}$$

The relations of the parameters (x, y) and (l, θ) are shown in Fig. 2.1. The resulting function $g(l, \theta)$ is commonly denoted as the sinogram. The Radon transform $\mathcal{R}$ maps the function f on $\mathbb{R}^2$ into the set of its integrals over the (x, y) plane. In other words, the transform maps the function f from the image domain (x, y) into the sinogram domain (l, θ). Traditionally, the function $g(l, \theta)$ has been viewed as a collection of one dimensional functions or projections $p_\theta(l)$ with the parameter θ (see Fig. 2.1).

In emission tomography, an important formulation of the Radon transform is the so called attenuated Radon transform [53], in which the attenuation of the tissue can be modeled and incorporated. A more general definition for this

transform is the weighted Radon transform, or the generalized Radon transform [7], defined as

$$g(l,\theta) \triangleq \mathcal{R}f = \int \int_{-\infty}^{\infty} w(x,y,l,\theta) f(x,y) \delta(x\cos\theta + y\sin\theta - l) dxdy, \quad (2.4)$$

where w is a weight function.

Properties of the Radon transform (Eq. 2.3) can be summarized as follows [29]. The Radon transform $\mathcal{R}$ is a linear mapping, and a total mass of the function $f(x,y)$ is preserved by $g(l,\theta)$ for all θ. If the function $f(x,y)$ is space–limited in (x,y), then the sinogram $g(l,\theta)$ is also space–limited in l. The projections $g(l,\theta)$ are periodic in θ with period 2π, and symmetric as $g(l,\theta) = g(-l,\theta \pm \pi)$. A (x_0,y_0) translation of the function f results in a shift of the sinogram g on the line as $g(l - x_0\cos\theta - y_0\sin\theta, \theta)$. A rotation of the function $f(x,y)$ by an angle θ_0 introduces a translation in θ as $g(l,\theta+\theta_0)$. A scaling of the (x,y) coordinates of f results in scaling of the l coordinate with an amplitude scaling of $g(l,\theta)$, that is $f(ax,by)$ results in $\frac{1}{|a|}g(al,\theta)$. The effects of object $f(x,y)$ motion in the sinogram domain (l,θ) are studied thoroughly in Ref. [51].

2.1.1 The Radon Transform Related Mappings

There are a few mappings which are closely related to the Radon transform. One such a mapping is the X–ray transform [53]. In two dimensional case, the Radon transform can be regarded as the X-ray transform, that is, the transforms are the same. In contrast, the n dimensional X–ray transform maps a function on $\mathbb{R}^n$ into the set of its line integrals, unlike the n dimensional Radon transform maps a function into a set of its integrals over the hyperplanes of $\mathbb{R}^n$ [53].

Another related mapping results in functions called linograms [17]. The linogram can be defined by mapping the function $g(l,\theta)$ into a new function as

$$\begin{aligned} q(c,d) \triangleq \mathcal{L}_d g &= \begin{cases} \frac{1}{1+d^2} g(\frac{c}{\sqrt{1+d^2}}, \tan^{-1} d), & \text{if } |d| < 1 \\ 0, & \text{otherwise} \end{cases} \\ q(c,d) \triangleq \mathcal{L}_c g &= \begin{cases} \frac{1}{1+c^2} g(\frac{d}{\sqrt{1+c^2}}, -\cot^{-1} c), & \text{if } |c| < 1 \\ 0, & \text{otherwise} \end{cases} \end{aligned} \quad (2.5)$$

where the values of the trigonometric functions are chosen such that $-\pi/4 < \tan^{-1} d < \pi/4$ and $\pi/4 < -\cot^{-1} c < 3\pi/4$. In the linogram domain, points which correspond to the line integrals through a fixed point of the object $f(x,y)$ form a trajectory of a straight line. In the sinogram domain, this trajectory for the fixed point is a sinusoidal curve (see Fig. 2.2). An extension of the (two

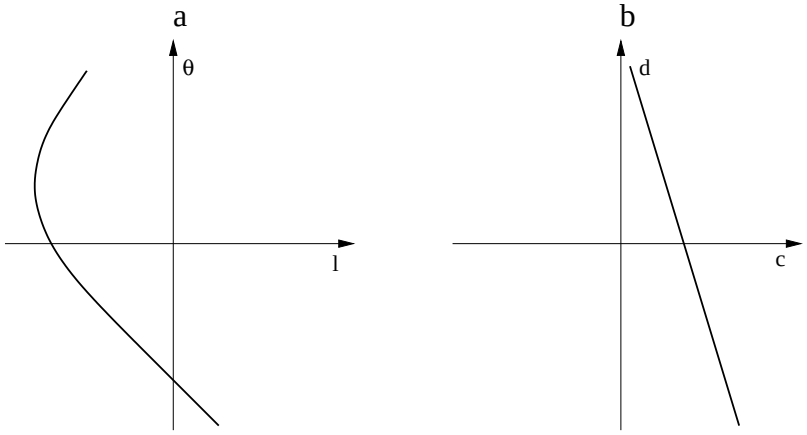

Figure 2.2: An illustration of the linogram domain: a) a sinusoidal trajectory of an (x, y) point in the sinogram domain (l, θ); b) the corresponding trajectory is a straight line in the linogram domain (c, d).

dimensional) linogram for a three dimensional object function is denoted as the planogram [8].

2.2 The Back–projection Operator

In this thesis, we are not considering in detail the inverse Radon transform in continuous case. A thorough definition for the inverse is presented e.g. in [53]. We review, however, the definition of the back–projection operator or the summation method, which is not an inverse of the Radon transform (Eq. 2.3) but its adjoint. The back–projection operator $\mathcal{B}$ represents the accumulation of all the projections of $g(l, \theta)$. This operator can be written as [29]

$$b(x, y) \triangleq \mathcal{B}g = \int_0^\pi g(x \cos\theta + y \sin\theta, \theta) d\theta. \tag{2.6}$$

The resulting function $b(x, y)$ is called the back–projection of $g(l, \theta)$, or the layergram[2] according to the term in Ref. [23]. The function $b(x, y)$ is a blurred image of $f(x, y)$. This blurring effect can be modeled by a point–spread function (PSF), whose inverse function gives a basis for the rho–filtered layergram reconstruction formula [23]. This formula provides a relationship between the

[2]Depending on a source of information the term layergram can also mean a back-projection for a fixed θ.

layergram $b(x, y)$ and the object function $f(x, y)$. That is, an inverse of the Radon transform can be obtained as $f = \mathcal{B}_\rho^{-1}(\mathcal{B}\mathcal{R}f)$, in which $\mathcal{B}_\rho^{-1}$ is the rho–filtered layergram reconstruction operator, $\mathcal{B}$ and $\mathcal{R}$ are the back–projection operator and the Radon transform, respectively.

2.3 The Projection Theorem

In the ill–posed reconstruction problem, the unknown object $f(x, y)$ or its distribution need to be recovered from the projections, since only the measured projections $g(l, \theta)$ of the object are known. In this section we review a fundamental theorem for image reconstruction from projections, giving the basis for discrete image reconstruction algorithms to be described.

The projection theorem or the Fourier slice theorem provides a relationship between the two dimensional Fourier transform of a function $f(x, y)$ and the one dimensional Fourier transform of its Radon transform or projections $p_\theta(l)$ for the angles θ. In other words, the one dimensional Fourier transform of $p_\theta(l)$ is equal to a slice of the two dimensional Fourier transform of the function $f(x, y)$ at the angle θ (see Fig. 2.3). This means that it is possible to recover the object from its measured projections by employing the two dimensional inverse Fourier transform for the filled two dimensional spectrum of $f(x, y)$.

The projection theorem can be formalized as follows. First, the two dimensional Fourier transform of the function $f(x, y)$ can be written as [32]

$$F(u, v) \triangleq \mathcal{F}_2 f = \int_{-\infty}^{\infty} \int_{-\infty}^{\infty} f(x, y) e^{-j2\pi(ux+vy)} dx dy. \tag{2.7}$$

Similarly, the one dimensional Fourier transform of the projections of the sinogram $g(l, \theta)$ can be defined as

$$G(w, \theta) \triangleq \mathcal{F}_1 g = \int_{-\infty}^{\infty} g(l, \theta) e^{-j2\pi wl} dl. \tag{2.8}$$

Now, according to the projection theorem (see Ref. [29] or [32]), the following relationship holds

$$G(w, \theta) = F(w \cos\theta, w \sin\theta), \tag{2.9}$$

where $u = w \cos\theta$ and $v = w \sin\theta$. The figure 2.3 illustrates this relationship for a fixed angle.

It can be noticed that if the function $f(x, y)$ is bandlimited, i.e. the Fourier transform is restricted to a finite range of frequencies as $F(u, v) = 0$ for $u^2 + v^2 > W^2$ [20], then also the projections $p_\theta(l)$ of $g(l, \theta)$ are bandlimited. This

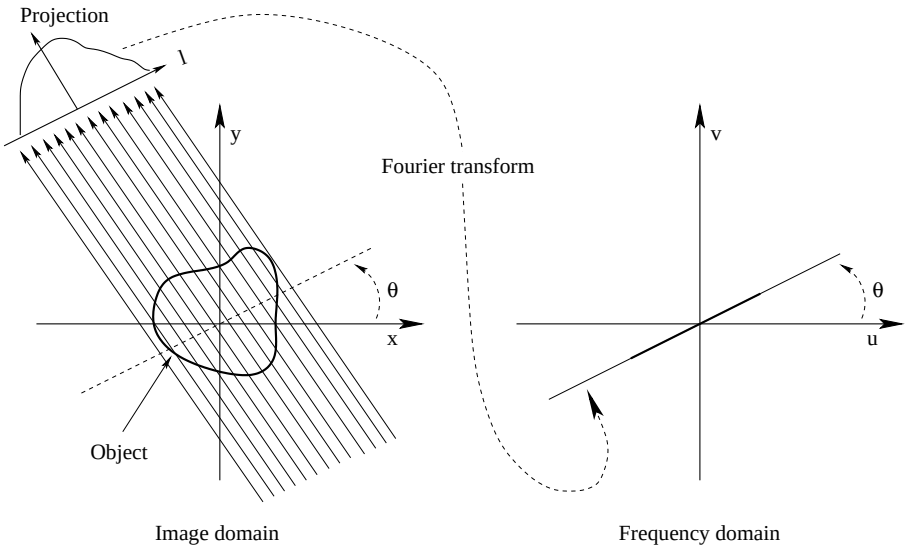

Figure 2.3: An illustration of the relationship between the one dimensional Fourier transform of the projection and the corresponding slice of the two dimensional frequency domain (u, v) of the object.

follows directly from the projection theorem (Eq. 2.9). This, however, does say very little about the two dimensional spectrum of $g(l, \theta)$, i.e. if the function $g(l, \theta)$ is regarded as a truly two dimensional or bivariate function [66]. In the discrete case, to be considered in the next chapter, this poses also an interesting question: "How many independent pieces of information about the function f can be found from M views?" [12]. The two dimensional interpretation of the sinogram can give an answer for the question.

Chapter 3

Image Reconstruction Algorithms

In practice the sinograms and the reconstructed images are represented as matrices, which are two (or higher) dimensional arrays. In this chapter we consider representation of the sinogram and its sampling in the discrete case. The filtered back–projection reconstruction algorithm is reviewed before discussion of iterative reconstruction algorithms, that are routinely employed nowadays.

3.1 Discrete Representation of Sinogram

A sinogram matrix represents a two dimensional cross–section of the measured object with the one dimensional projections. The horizontal row of the sinogram refers to radial samples, and the vertical column to angular views (see Fig. 3.1). The projections at different angles are available on a finite grid, not on a continuous space as in the real world. Therefore, the limitations of the discrete representations need to be taken into account, like in any digital application of discrete signals.

Often, the following two assumptions about the object f are made: 1) it is space limited i.e. $f(x, y) = 0$ for $x^2 + y^2 > R^2$; and 2) bandlimited i.e. $F(u, v) = 0$ for $u^2 + v^2 > W^2$. Thereby, the discrete sinogram $\mathbf{g}$ can be written as [29]

$$\mathbf{g}(l_n, \theta_m) \triangleq [\mathcal{R}f](l_n, \theta_m), \tag{3.1}$$

where $-N/2 \leq n \leq N/2 - 1$ and $0 \leq m \leq M - 1$. The support regions R and W are illustrated in Fig. 3.2. Since the energy of the frequencies in the Fourier domain is zero above the bandlimited frequency W, also the projections $\mathbf{p}_\theta(l_n)$ of $\mathbf{g}$ can be considered as bandlimited signals.

The sampling interval Δ_l for the projections in the l direction for each θ should satisfy $\Delta_l < 1/(2W)$, according to the sampling theorem. Thus, the

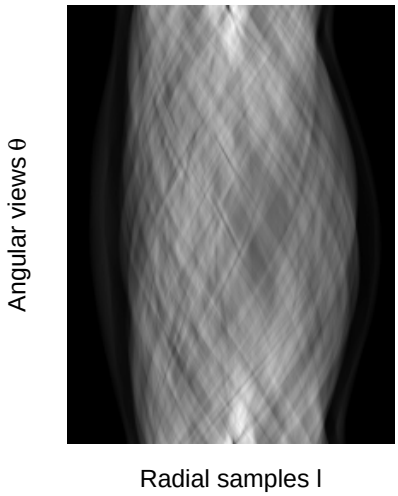

Figure 3.1: A noiseless sinogram.

following holds $2R = N\Delta_l$, since $\mathbf{p}_\theta(l_n)$ is zero for $|l_n| > R$, and the required minimum number of samples for the projections is [66]

$$N = 4RW. \tag{3.2}$$

Obtaining the minimum sampling rate in the θ direction of the sinogram is not so straightforward, because of the periodicity of the sinogram [66]. However, by restricting the angular view for the interval $\theta_m \in [0, \pi)$, or $\theta_m \in [0, \pi[$, the minimum sampling rate can be derived. Besides, the sinogram $\mathbf{g}(l_n, \theta_m)$ is often regarded as a "continuous" function in l, and then by founding on the projection theorem, the required minimum sampling rate in θ can be set. In Ref. [66], it is shown that $G(w, \theta)$ of Eq. 2.9 is bandlimited to $RW + 1$ with respect to θ for each $w \in [-W, W]$. Hence, the sampling interval in the θ direction must satisfy $\Delta_\theta < \frac{1}{2(RW+1)}$. According to Ref. [66], the required minimum number of equally spaced samples over $[0\ \pi)$ in the θ direction is

$$M = 2\pi(RW + 1). \tag{3.3}$$

The above minimum numbers of samples in the l and θ directions (Eq. 3.2 and 3.3) specify the Radon transform in the (l, θ) domain on a rectangular grid. The sinogram $\mathbf{g}(l_n, \theta_m)$ is considered as a collection of one dimensional functions with the parameter θ[1]. This can be regarded as a traditional viewpoint of the sinogram domain, as mentioned. However, if the sinogram is regarded as

[1]The projection theorem (Eq. 2.9) says that the Fourier transform of the one dimensional

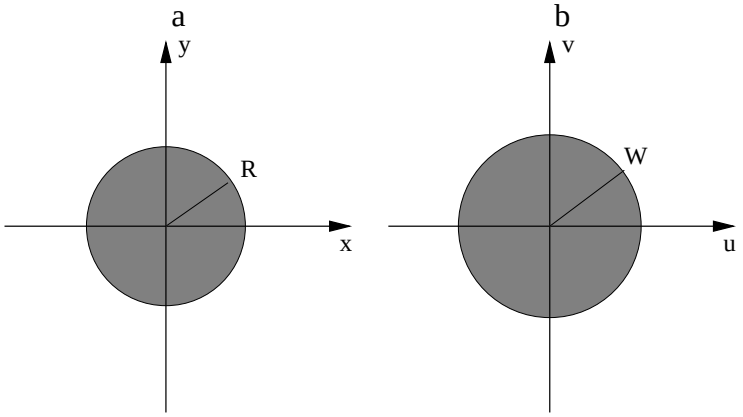

Figure 3.2: Support regions. In a), an R–disk support region for $f(x, y)$. The support region can be regarded as a field of view (FOV) as well. In b), a W–disk support frequency region for $F(u, v)$.

a fully two dimensional function, its (two dimensional) spectrum is not theoretically exactly bandlimited, due to the periodicity of the sinogram. In other words, the sinogram is "quasi–bandlimited", that is, the spectrum can be regarded to be bandlimited from a practical standpoint [60]. The total number of independent pieces of information that can be extracted from the discrete sinogram g is approximately $\frac{2}{\pi}N^2$, which can be derived if the sinogram is regarded as quasi–bandlimited [66]. Some authors have also studied sampling for the Radon transform of "finite complexity objects", i.e. the function f contains simple fragments only [50].

3.2 Implementation of Back–Projection

In the discrete case, the back–projection operator $\mathcal{B}$ (Eq. 2.6) can be implemented by replacing the integral with a Riemann sum and employing interpolation. We use Δ_θ to denote the interval of angular samples, and Δ_l the interval of radial samples, as we describe above. The approximation of the

projection at the angle θ is a slice of the two dimensional Fourier transform of the object $f(x, y)$. Thus, we can say that the projections are (nearly) independent in the filled two dimensional Fourier spectrum, since the DC component is the only common information at the different angles [32].

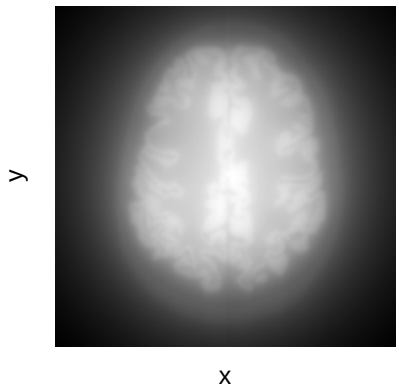

Figure 3.3: A back–projected image from the sinogram shown in Fig. 3.1. The image is considerably blurred as can be noticed.

back–projection operator (Eq. 2.6) can be written as [29]

$$\mathbf{b}(x_i, y_j) = \mathcal{B}_M \mathbf{g} \triangleq \Delta_\theta \sum_{m=0}^{M-1} \hat{\mathbf{g}}(x_i \cos \Delta_\theta m + y_j \sin \Delta_\theta m, \Delta_\theta m), \qquad (3.4)$$

where $-N/2 \leq i, j \leq N/2 - 1$, $\mathcal{B}_M$ is the discrete back–projection operator, and $\hat{\mathbf{g}}$ is an estimated sinogram. The estimation is done by interpolation [75] from the known values of $\mathbf{g}(l_n, \theta_m)$, since the values for the resulting back–projection with the sampling interval of Δ_l at the points $-N/2 \leq n \leq N/2 - 1$ need to be known accurately. Linear interpolation or different spline interpolators [39] are commonly employed for the task. A back–projected image is shown in Fig. 3.3.

In practice, the discrete back–projection operator (Eq. 3.4) can be implemented using image rotations. In other words, each projection $\mathbf{p}_\theta(l_n)$ is back–projected at zero angle to a matrix of size $N \times N$, followed by a rotation of θ, and then the rotated matrices are summed up together resulting in intensity values of $\mathbf{b}(x_i, y_j)$.

The formulation (Eq. 3.4) is analogous to the continuous equation (Eq. 2.6). Still, there exist various discrete implementation possibilities for the back–projection. One such an implementation can be expressed in the matrix notation from a vectorized sinogram $\mathbf{y}$ into a vectorized back–projected image $\mathbf{x}$ as [32]

$$\mathbf{x} = \mathbf{B}^T \mathbf{y}, \qquad (3.5)$$

in which T denotes the matrix transpose. The matrix $\mathbf{B}$ is often denoted as the system matrix. Furthermore, the matrix with the transpose is commonly

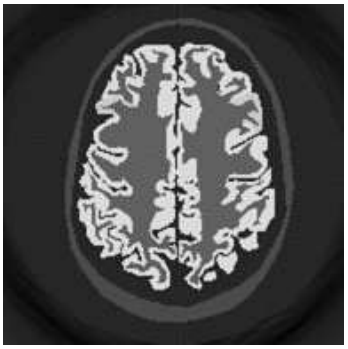

Figure 3.4: An FBP–reconstructed image. See also the corresponding sinogram (Fig. 3.1) and back–projected image (Fig. 3.3).

considered as the discrete back–projection [24]. In the system matrix notation, a line integral (or sum) contributes only to those pixels which it intersects, not to others (or so it is expected) . In contrast, in the approximation of the continuous back–projection operator (Eq. 3.4) the line integral might contribute to other pixels also, because of interpolation errors.

3.3 The Filtered Back–Projection Algorithm

The filtered back–projection (FBP) algorithm can be viewed as a discrete implementation of the inverse Radon transform. Still nowadays, the FBP algorithm is a widely used image reconstruction method because it is linear, fast, and straightforward to implement, although it has some well–known drawbacks. The FBP algorithm can be written as [29]

$$\mathbf{f}(x_i, y_j) \triangleq \mathcal{B}_M \mathcal{H} \mathbf{g}(l_n, \theta_m), \tag{3.6}$$

where $\mathcal{B}_M$ is the discrete back–projection operator (Eq. 3.4) and $\mathcal{H}$ is a one dimensional filter. The filter $\mathcal{H}$ represents a deblurring operator for the smoothing introduced by back–projection (see Fig. 3.3). The FBP algorithm is numerically stable, although the inversion of the Radon transform is an ill–posed problem. The reconstructed image $\mathbf{f}$ represents reliably the true measured object, without assuming any *a priori* information on the object. Let $\mathbf{G}(w_n, \theta_m)$ be the one dimensional Fourier transform of the projections (Eq. 2.8) and let W_n^b be the frequency response of the high–pass filter $\mathcal{H}$ with a cut–off frequency of b.

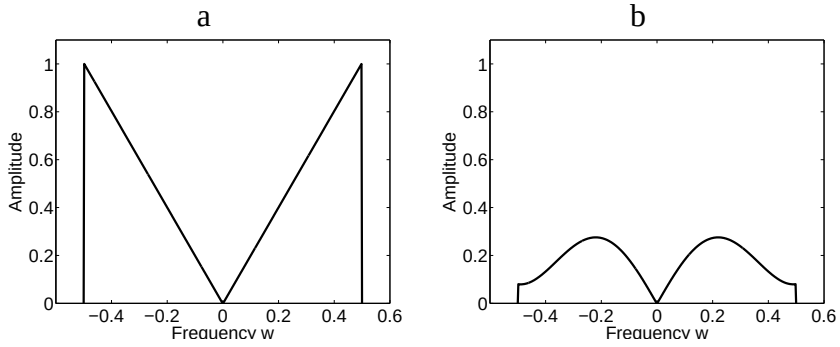

Figure 3.5: In a), the frequency response W_n^b of the FBP ramp filter $\mathcal{H}$. In b), the ramp filter is multiplied by the Hamming window. The cut–off frequency b is 0.5 (i.e. the Nyqvist frequency) in both cases.

Then the filter $\mathcal{H}$ can be expressed as

$$\tilde{\mathbf{g}} \triangleq \mathcal{H}\mathbf{g} = \mathcal{F}_1^{-1}(W_n^b \mathcal{F}_1 \mathbf{g}) = \mathcal{F}_1^{-1}(W_n^b \mathbf{G}(w_n, \theta_m)), \tag{3.7}$$

where $\mathcal{F}_1$ denotes the one dimensional Fourier transform. The FBP algorithm simply filters the projections of the sinogram $\mathbf{g}$ in the frequency domain and then back–projects the resulting sinogram $\tilde{\mathbf{g}}$ into the reconstructed image $\mathbf{f}$ (Eq. 3.6). An FBP reconstructed image is shown in Fig. 3.4. The frequency response of the filter $\mathcal{H}$, which is called the Ram–Lak or ramp filter, is shown in Fig. 3.5(a). A similar algorithm to the FBP method is the convolution back–projection (CBP) algorithm, in which the deblurring filter is implemented in a different way compared to FBP. Worth noticing is that FBP and CBP are totally different algorithms in comparison with the direct Fourier reconstruction method (based on Eq. 2.9) or the rho–filtered layergram method [23], that are mentioned in the previous chapter.

A crucial parameter in the algorithm is the cut–off frequency b, which controls the resolution. The object function from which the sinogram $\mathbf{g}$ is obtained should be space limited and b – band–limited in order to reconstruct the image reliably [53]. The high–pass filter $\mathcal{H}$ emphasizes the higher frequencies in order to provide a sharp image (compare Fig. 3.3 and Fig. 3.4). This, however, is also the problem of the FBP method, since often in practical applications the noise component introduced by the image acquisition process consists of high spatial frequencies. Therefore, the high frequency noise is amplified relatively more than the other lower spatial frequencies in the reconstructed image. Basically, a lower cut–off frequency b introduces worse resolution in the FBP image, but then high frequency noise can be reduced. Often, instead of using rough cut–off

for the frequency response (Fig. 3.5(a)), the ramp filter is multiplied by a window function in the presence of noise. This provides a better trade–off between the resolution and noise reduction. A possible choice for the window function is for example the Hamming window (see Fig. 3.5(b)).

3.3.1 Other Reconstruction Algorithms

There exist several different image reconstruction algorithms, although the above described FBP method is perhaps most well–known. Next we describe a few of the reconstruction algorithms briefly, in order to clarify that there are also different approaches for image reconstruction. The reconstruction algorithms can be divided roughly into two categories: analytical methods and iterative techniques.

Analytic or Transform Based Reconstruction

Image reconstruction can be implemented as a discretized version of the projection theorem (Eq. 2.9). That is, the two dimensional spectrum of the image is filled by the one dimensional spectrums of the projections prior to the two dimensional inverse Fourier transform. This method is called the direct Fourier method. The method obviously suffers from interpolation artifacts in the frequency domain, in which interpolation should be performed extremely accurately. Still, some improvements for the method have been published recently [89]. Another closely FBP related reconstruction method is the rho–filtered layergram method, which is briefly described in the previous chapter already. In this reconstruction technique, the sinogram is first back-projected and then multiplied by a two dimensional filter in the two dimensional frequency domain. This method, however, has some theoretical problems and therefore it is not used much [53]. Still, the rho–filtered reconstruction method can be found useful in stackgram applications, described in the following chapters. The direct Fourier method, the rho–filtered layergram method, FBP, and CBP can be considered as analytic or transform based methods [43].

Iterative Reconstruction Algorithms

Several iterative reconstruction algorithms based on solving linear equations have been introduced. Iterative reconstruction algorithms can be further divided into (at least) three classes [85]: 1) conventional iterative algebraic methods, 2) iterative statistical methods, and 3) iterative filtered back-projection algorithms. We next discuss shortly the first two of the methods. The first class of iterative

methods includes the algebraic reconstruction technique (ART). In ART, it is necessary to know the line integral paths that connect the "transmitter" and the "receiver" (see Fig. 2.1). This relationship can be presented with the system matrix notation (Eq. 3.5). The reconstructed image is solved iteratively from the linear equations. This iterative procedure is known as Kaczmarz's method in the literature [53]. Different algebraic techniques (e.g. SIRT, LWB, etc. [85]) employ different modeling for the linear equations.

Basically, the iterative statistical algorithms reconstruct the images by maximizing a likelihood function related to the measurement. In PET, a widely used statistical image reconstruction method employs maximum likelihood estimation via expectation maximization (MLEM) [42]. The Poisson nature of photon counting (such as in PET) fits without difficulty for the maximum likelihood approach. The idea of the algorithm can be summarized as follows. Let $\mathbf{y}$ be an observed (or measured) random vector. Let the vector $\mathbf{y}$ has a density function $\tau(\mathbf{y}, \phi)$, where ϕ is a vector of parameters to be estimated. Maximization of $\tau(\mathbf{y}, \phi)$ with respect to ϕ may be difficult. Therefore, the expectation maximization algorithm postulates another random vector, say $\mathbf{x}$, to have a mapping $\mathbf{y} = \Phi(\mathbf{x})$. The vector $\mathbf{x}$ is supposed to have a density function $\eta(\mathbf{x}, \phi)$ with respect to a measure $\theta(\mathbf{x})$. Thus, the density function $\tau(\mathbf{y}, \phi)$ can be recovered as $\tau(\mathbf{y}, \phi) = \int_\Omega \eta(\mathbf{x}, \phi) d\theta(\mathbf{x})$, where $\Omega = \{\mathbf{x} : \mathbf{y} = \Phi(\mathbf{x})\}$ [42]. In the discrete case, the equation is solved iteratively in two steps. First, a conditional expectation is formed (the so called E–step). Secondly, the conditional expectation is maximized with respect to the variable ϕ (M–step). The standard MLEM algorithm is suitable for Poisson distributed data. The method, however, can be also employed for non–Poisson data with the noise equivalent count (NEC) transformation [54].

Another important concept in statistical reconstruction is maximum–a– posteriori (MAP) estimation [22]. The MAP estimation is based on MLEM, but the MAP method takes into account prior information about "smoothness" of the object. In the MAP algorithm, the M–step of the MLEM method is replaced by maximization of the posterior probability employing a prior function. For example, the MRP algorithm [1] can be categorized to be a MAP (or a regularized MLEM) reconstruction method, in which the prior term is regarded as a "median root". The MRP algorithm is a good example of such an iterative reconstruction method which can, in the presence of noise, reconstruct the image more reliably than the FBP method, which is extremely sensitive to noise.

Statistical image reconstruction can be seen as a parameter estimation problem. The statistical algorithms are based on a realistic description of the noise. Therefore, accurate models of image formation process can be incorporated resulting in quantitative reconstruction. *A priori* knowledge about the object as

well as sophisticated regularization methods can be exploited in the algorithms. This also explains the reason why these methods are so popular nowadays, especially in PET studies.

Chapter 4

Decomposition of Sinogram into Stackgram

The main topic of this thesis is the novel stackgram domain, to be defined next. In this chapter, we present the definitions of the stack operator and its inverse in the continuous case. These operators map the sinogram into the stackgram, and vice versa. The operators are fairly simple and they are based on the notations presented in the previous chapters. We also present the discrete implementations of the stackgram operators, namely the discrete stack operator and its inverse.

4.1 The Stack Operator and its Inverse

The stack operator back–projects each projection $p_\theta(l)$ of the sinogram $g(l, \theta)$ over the (x, y) plane into a set of the back–projections resulting in a three dimensional function, namely the stackgram. This can be formalized as [P-1]

$$h(x, y, \theta) \triangleq \mathcal{S}g(l, \theta) = g(x \cos\theta + y \sin\theta, \theta). \tag{4.1}$$

As it can be noticed, the (x, y) layers of the stackgram are constant or redundant along each θ angle. Therefore, it is normally reasonable to bound the range of the stack operator as $\{h(x, y, \theta) = 0 \mid x^2 + y^2 > C^2$ and $\theta \notin [0\ \pi)\}$, or use e.g. a so called mollifier function [62] for the bounding. The stack operator $\mathcal{S}$ seems to be similar to the back–projection operator (Eq. 2.6). Actually, the only difference is that the integral of the back–projection operator $\mathcal{B}$ is replaced by the third dimension θ of $h(x, y, \theta)$. The function $h(x, y, \theta)$ can be considered as a stack of back–projected projections with the parameter θ, in the similar way as the sinogram $g(l, \theta)$ is often regarded as a collection of the one dimensional

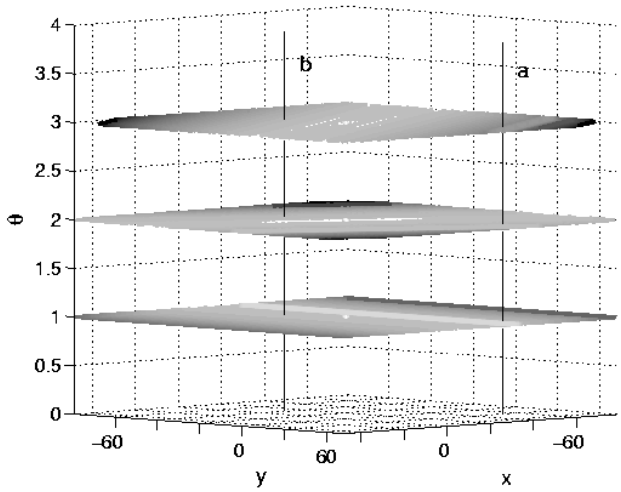

Figure 4.1: An illustration of the stackgram $h(x, y, \theta)$ consisting of back–projected projections. The signals along the sinusoidal trajectories (Fig. 1.1) of the sinogram $g(l, \theta)$ are decomposed in the stackgram domain, and are denoted as the locus–signals $h_{(x,y)}(\theta)$. The lines **a** and **b** depict different locations of two sinusoidal trajectory signals of the sinogram in the stackgram. See also the corresponding locus–signals in Fig. 4.2.

projections. The two dimensional (x, y) layers of the stackgram are sometimes denoted as ridge functions [36], introduced already in 1975 by Logan and Shepp as $r(x, y) = r(x \cos\theta + y \sin\theta)$. The ridge functions, however, are only two dimensional functions, in contrast to the three dimensional stackgram $h(x, y, \theta)$.

The stackgram domain (x, y, θ) enables decomposition of different curves consisting of the values along the sinusoidal trajectory signals of the sinogram (Fig. 4.1). This is the function of the stackgram approach; to offer an environment to independently process the signals along the sinusoidal trajectories of the sinogram. These signals, denoted as the locus–signals in the stackgram domain, are as

$$h_{(x,y)}(\theta) = h(x, y, \theta), \quad \forall\ (x, y) \in \{x^2 + y^2 \leq C^2\} \subset \mathbb{R}^2. \tag{4.2}$$

Selected locus–signals are shown in Fig. 4.2.

The stackgram domain can be regarded as an intermediate form of the sinogram (l, θ) and image (x, y) domains, having features from the both domains. Besides, the stackgram $h(x, y, \theta)$ can be mapped into the image or sinogram domain by simple operations. For example, if the stackgram $h(x, y, \theta)$ is inte-

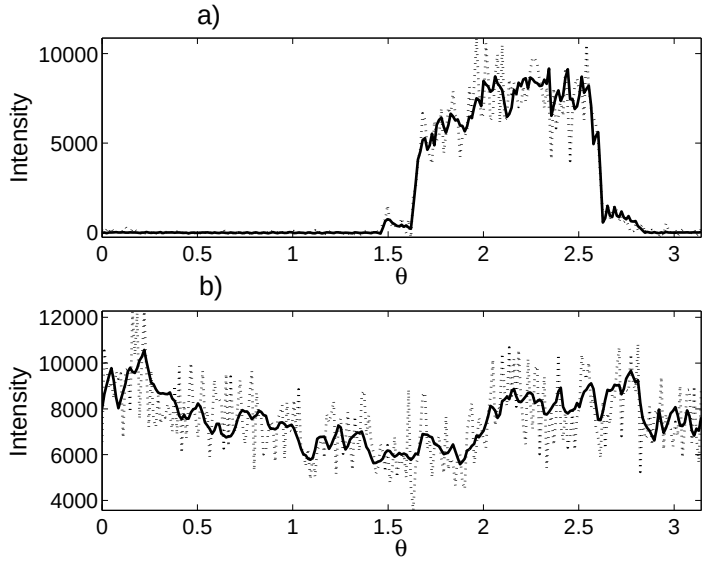

Figure 4.2: Locus–signals at different spatial (x, y) locations. The signals with dotted line represent noisy locus–signals, whereas noise–free locus–signals are shown with solid line. The lines **a** and **b** in Fig. 4.1 depict the different spatial locations of the signals. The locus–signals in a), depicted by the line **a**, do not have significant accumulation of the projections for all the angles. In b), on the other hand, the locus–signals are formed at the spatial position depicted by the line **b** having accumulation of the full range of views. The noiseless object function $f(x, y)$ of the locus–signals is shown in Fig. 3.4.

grated along the θ axis, the resulting function is the layergram $b(x, y)$, which can be restored back to $f(x, y)$. This intermediacy means also that the properties of the stack operator are a certain mixture of the image and sinogram domain properties [29]. The most important properties, that are exploited in this work, are presented in Table 4.1. Some of these properties are considered in [P-4] and [P-5] as well. The stack operator, like the Radon transform, is a linear mapping, therefore the shown properties are fairly straightforward to derive.

The inverse stack operator is a mapping from the stackgram domain (x, y, θ) into the sinogram domain (l, θ). This inverse operator is not unique, because of the redundancy of the (x, y) layers of the stackgram (i.e. the layers are constant along each angle θ). A possible inverse $\mathcal{S}^{-1}$ can be expressed by the simple

	Object	Sinogram	Stackgram
	$f(x,y)$	$g(l,\theta)$	$h(x,y,\theta)$
Linearity:	$af_1(x,y)+bf_2(x,y)$ a_1 and a_2 constants	$ag_1(l,\theta)+bg_2(l,\theta)$	$ah_1(x,y,\theta)+bh_2(x,y,\theta)$
Periodicity:	$f(x,y)$	$g(l,\theta)=g(l,\theta+2k\pi)$ k is integer	$h(x,y,\theta)=h(x,y,\theta+k\pi)$
Shift:	$f(x-x_0,y-y_0)$	$g(l-x_0\cos\theta-y_0\sin\theta,\theta)$	$h(x-x_0,y-y_0,\theta)$
Rotation:	$f_p(r,\phi+\theta_0)$ in polar coordinates	$g(l,\theta+\theta_0)$	$h_p(r,\phi+\theta_0,\theta+\theta_0)$

Table 4.1: Properties of the stackgram $h(x,y,\theta)$ with respect to the object $f(x,y)$ and the sinogram $g(l,\theta)$.

relations $x = l\cos\theta$ and $y = l\sin\theta$ as [P-2]

$$g(l,\theta) \triangleq \mathcal{S}^{-1}h = h(l\cos\theta, l\sin\theta, \theta). \tag{4.3}$$

It can be verified that $g = \mathcal{S}^{-1}(\mathcal{S}g)$.

The expression of Eq. 4.3, however, is not feasible for practical stackgram applications, in which case the locus–signals (Eq. 4.2) are modified by an operator (such as a filter). A more appropriate inverse $\mathcal{S}_w^{-1}$ can be defined by the following equation as [P-2]

$$g(l,\theta) \triangleq \mathcal{S}_w^{-1}h = \int\int_{-\infty}^{\infty} w(x,y,l,\theta)h(x,y,\theta)\delta(x\cos\theta + y\sin\theta - l)dxdy, \tag{4.4}$$

where w is a weight function. The definition (Eq. 4.4) is denoted as the generalized inverse stack operator. In Eq. 4.4, the generalized Radon transform (Eq. 2.4) maps each (x,y) layer of the stackgram $h(x,y,\theta)$ with the weight function w into a projection of $g(l,\theta)$ at the angle θ.

4.2 Discrete Stackgram

The discrete back–projection (Eq. 3.4) is a direct dicretized form of the continuous back–projection operator (Eq. 2.6). In a similar way, a discrete formulation for the stack operator $\mathcal{S}$ could be implemented according to the continuous definition (Eq. 4.1) directly. Another formulation for the discretized stack operator could be obtained using the system matrix notation (Eq. 3.5). However, we want to present a discrete formulation of the stackgrams using image rotations, in such a manner that the transformation from the sinogram $\mathbf{g}$ into the stackgram $\mathbf{h}$ is reversible. That is, the back and forth transformations (with image

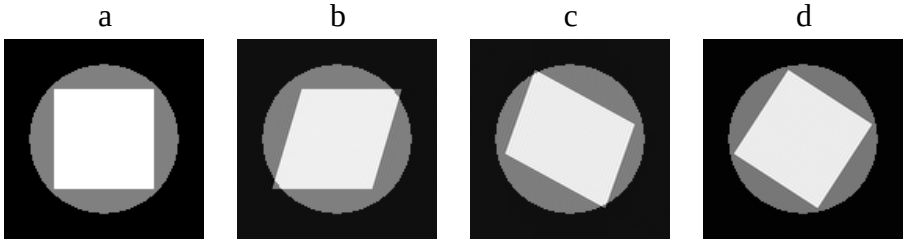

Figure 4.3: An illustration of the three–pass rotation: a) an initial square in the image. In b), c), and d), the square after the first, second, and third pass. The shown disk is not rotated along the square, but the disk emphasizes the maximum region (or FOV) in which the rotated image can be formed after the three passes. Due to the three–pass algorithm, the size of the resulting rotated image need to be bigger than the initial one (black represents the required extra size).

rotations) result in errors which are mainly caused by the numerical accuracy of computer arithmetic. In order to achieve this requirement, we consider implementations for the stack operator and its inverse by using three–pass image rotations with sinc–interpolation. We review the three–pass rotation algorithm and sinc–interpolation before the definitions for the discrete stack operator and its inverse.

4.2.1 Three–Pass Rotation with Sinc–Interpolation

Often image rotation is obtained by spline interpolation to estimate the rotated coordinates. In contrast to this traditional spline based image rotation procedure, the image rotation can be decomposed into three one dimensional translations. This can be implemented using sinc–interpolation, to be defined below, in such a manner that the translations (and therefore the image rotation) are reversible. Three–pass rotation can be written as [81]

$$\begin{aligned} Rotate(\theta) &= \begin{bmatrix} \cos\theta & -\sin\theta \\ \sin\theta & \cos\theta \end{bmatrix} \\ &= \begin{bmatrix} 1 & -\tan\theta/2 \\ 0 & 1 \end{bmatrix} \cdot \begin{bmatrix} 1 & 0 \\ \sin\theta & 1 \end{bmatrix} \cdot \begin{bmatrix} 1 & -\tan\theta/2 \\ 0 & 1 \end{bmatrix}. \end{aligned} \tag{4.5}$$

These three–step translations for image rotation (see Fig. 4.3) can be implemented by convolution with the sinc–kernel. Furthermore, since convolution

corresponds to multiplication in the frequency domain, the fast Fourier transform (FFT) can be employed for the translations to multiply the spectrum by the interpolation kernel.

The support of sinc–interpolator is infinite (unlike the supports of spline interpolators), meaning that the number of data samples should be infinite too. However, discrete signals have always a limited number of samples and therefore a truncated sinc–function is applied for interpolation, instead of the infinite length sinc–kernel. The truncated sinc–function (or truncated Fourier series) is associated to the well–known Gibbs phenomenon or ringing effect. In this thesis, we are not considering the traditional sinc–kernel, but a numerically stable form of it in order to reduce the ringing effect. The numerical stable sinc–interpolator (i.e. the discrete sinc–interpolator [86]) is mathematically equivalent to the Fourier or Dirichlet kernel [16]. This stable form is slightly modified for our purposes to be reversible for signals of even number samples. Worth noticing is that we are not employing sinc–interpolation for increasing the samples, but shifting the signals in three–pass rotation.

The applied discrete sinc–interpolator with a shift parameter $s \in \mathbb{R}$ can be expressed in the Fourier domain as [86]

$$\eta^{s}_{w,odd} = \begin{cases} \exp(\frac{i2\pi sw}{N}) & \text{if } w = 0, \ldots, \frac{N-1}{2} \\ \exp(\frac{i2\pi s(w-N)}{N}) & \text{if } w = \frac{N-1}{2}+1, \ldots, N-1 \end{cases}, \tag{4.6}$$

when the number of samples N is odd. In the case of the even number of samples, the sinc–interpolator kernel [86] is not exactly reversible, because the highest frequency component $\frac{N-1}{2}$ is slightly modified. However, since we are applying sinc–interpolation only for translations of the signals, we can accept aliasing of the highest frequency component (assuming that the data are properly sampled). Thus, the sinc–kernel can be rewritten for even number samples N as [P-2]

$$\eta^{s}_{w,even*} = \begin{cases} \exp(\frac{i2\pi sw}{N}) & \text{if } w = 0, \ldots, \frac{N-1}{2}-1 \\ 1 & \text{if } w = \frac{N-1}{2} \\ \exp(\frac{i2\pi p(w-N)}{N}) & \text{if } w = \frac{N-1}{2}+1, \ldots, N-1. \end{cases} \tag{4.7}$$

It is easy to verify that $\eta^{s}_{w,odd}\eta^{-s}_{w,odd} = 1$ and $\eta^{s}_{w,even*}\eta^{-s}_{w,even*} = 1$. This means that image rotation with the three–pass rotation algorithm (Eq. 4.5) and the interpolators is reversible. Besides, the quality of rotated images is good, although the ringing effect near high edges of rotated data can be introduced. This Gibbs phenomenon could be reduced by using a different transform, such as the discrete cosine transform (DCT) instead of the Fourier transform, for the interpolation [87, 88].

4.2.2 The Discrete Stack Operator

As mentioned above, the discrete stack operator is reversible, if the sinogram $\mathbf{g}$ is bandlimited and the three–pass rotation algorithm (Eq. 4.5) with sinc–interpolation (Eq. 4.6 or 4.7) is employed. Let $\mathbf{g}_{\theta_m}$ denote a row vector of the sinogram (Eq. 3.1) at the angle θ_m. A back–projection at zero angle (to be rotated by the angle θ_m) can be defined then as

$$\mathbf{p}(x_i, y_j) = [\mathbf{g}_{\theta_m}^T, \mathbf{g}_{\theta_m}^T, \ldots, \mathbf{g}_{\theta_m}^T]^T. \tag{4.8}$$

The back–projection $\mathbf{p}$ is an $N \times N$ matrix. The discrete stackgram $\mathbf{h}$ can be generated simply by stacking the replicated sinogram rows $\mathbf{p}$ followed by three–pass rotation $rot(\cdot, \cdot)$ for the angles θ_m as [P-2]

$$\mathbf{h}(x_i, y_j, \theta_m) = rot(\mathbf{p}(x_i, y_j), \pi/2 - \theta_m). \tag{4.9}$$

In three–pass rotation, the range of views $[0 \ \pi)$ is replaced by the range of $[-\pi/2 \ \pi/2)$. Otherwise the translations in three–pass rotation are too large for practical purposes. Besides, the sides of the rotated image (or the stackgram layers) would be too much mirrored due to the mirroring effect introduced by the discrete Fourier transform in the translations [81]. Therefore, the region in which the rotated image is formed can be regarded as a circular region having a radius of $s \leq 3N/8$, where N denotes the number of the sinogram bins. In Fig. 4.3, the grey circular region (having the radius of s) illustrates this "support" or FOV region in the three–pass rotation. The locus–signals $\mathbf{h}_{\theta_m}$ are formed only inside this region. Therefore, the spatial size of the stackgrams need to be usually increased by zero padding the projections as $\hat{\mathbf{g}}_{\theta_m} = [0, \ldots, 0, \mathbf{g}_{\theta_m}, 0, \ldots, 0]$. In this way the stackgram "support" area corresponds to the support of the reconstructed image (Fig. 3.2), if the three–pass rotation is employed. Specifically, the size of the discrete stackgram is then increased as $-2N/3 \leq i, j \leq 2N/3$.

When the projections of the sinogram $\mathbf{g}(l_n, \theta_m)$ are sampled according to the sampling theorem (Eq. 3.2), the (x_i, y_i) layers of the stackgram $\mathbf{h}$ are also band–limited, since the one dimensional projections are simply duplicated at the angles θ_m. However, the meaning of sampling along the stackgram angular θ_m axis is not that obvious. In other words, the length of the sinusoidal trajectory for a spatial (x, y) point at radius of R (see R in Fig. 3.2) is longer than for a point at near the origin $r = 0$. Furthermore, the sampling rate in the angular direction θ of the sinogram is fixed for all the spatial points. This results in different resolution for the signals along the sinusoidal trajectories (see Fig. 4.4). Under certain assumptions, it can be shown that a discrete estimate of the object function $f(x, y)$ can be reconstructed with twice the resolution in

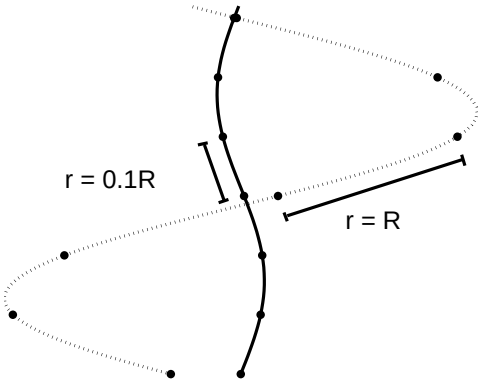

Figure 4.4: The difference of signal lengths along the sinusoidal trajectories in the sinogram domain. Near the origin ($r = 0.1R$) of the image $f(x, y)$, the length between the sampling points along the sinusoidal trajectories of the sinogram is much shorter than at $r = R$.

the region near the origin $r = 0$ as at $r = R$ [66]. This indicates also that the locus–signals in the stackgram have better resolution near the origin $r = 0$ than at $s = 3N/8 = R$.

4.2.3 The Discrete Inverse Stack Operator

The discrete inverse stack operator can be implemented in a similar manner as the discrete stack operator (Eq. 4.9) by employing the three–pass rotation algorithm with sinc–interpolation. Let the operators $\odot$ and $\cdot$ define the element by element multiplication of matrices and the normal matrix multiplication, respectively. Let the matrix $\mathbf{O}$ be a matrix of size $N \times N$ of zeros and ones forming a circular disk (or the "support") of ones with radius of $3N/8$ (which corresponds to the grey circle in Fig. 4.3). Then, a cumulative vector can be defined as $\mathbf{r} = [1_1, 1_2, \ldots, 1_N] \cdot \mathbf{O}$, and the elements of a weight vector $\mathbf{w}$ can be written as

$$w_i = \begin{cases} 1/r_i, & \text{if } r_i \neq 0 \\ 0, & \text{otherwise} \end{cases} . \tag{4.10}$$

The vector $\mathbf{w}$ corresponds to a possible choice for the weight function $w(x, y, l, \theta)$ in Eq. 4.4. The kth row of the sinogram $\mathbf{g}(l_n, \theta_m)$ can then be defined as [P-2]

$$\mathbf{g}_k = \mathbf{w} \cdot (rot(\mathbf{h}(x_i, y_i, \theta_k), \theta_k - \pi/2) \odot \mathbf{O}). \tag{4.11}$$

The final sinogram $\mathbf{g}$ from the discrete stackgram $\mathbf{h}$ can be constructed as

$$\mathbf{g}(l_n, \theta_m) = [\mathbf{g}_1^T, \mathbf{g}_2^T, \ldots, \mathbf{g}_k^T, \ldots, \mathbf{g}_M^T]^T. \tag{4.12}$$

If the projections were zero–padded as $\hat{\mathbf{g}}_{\theta_m}$, the padded elements can be omitted in Eq. 4.12. It can be verified that the forth and back transformation of a discrete sinogram matrix $\mathbf{g}$ by using the discrete stack operator (Eq. 4.9) and its inverse (Eq. 4.11) produce errors that can be interpreted as roundoff errors caused by the numerical accuracy of computer arithmetic.

Chapter 5

Filtering of Sinogram Data

Noise reduction is a relevant issue especially in emission tomography due to the low signal–to–noise ratio. In the thesis, we concentrate on comparisons of different filtering directions in the sinogram and stackgram domains. Our purpose is not to study the best possible selection of the filters for each direction. In this chapter, we review only some basic principles of filtering in the sinogram domain, giving a motivation for filtering of the data in the stackgram domain.

5.1 Radial and Angular Directions

As it is stated, image reconstruction is an ill–posed problem making the reconstruction methods sensitive to noise. The noise component contains usually high frequencies and therefore it tend to be amplified relatively more than the other components of the data due to reconstruction. Thus, it would be preferable to perform noise reduction before image reconstruction, although some reconstruction algorithms can reduce noise efficiently during the reconstruction process. Radial filtering (i.e. filtering along the projections (see Fig. 3.1)) of the sinogram data $\mathbf{g}(l_n, \theta_m)$ is commonly applied with various filters to attenuate the high–frequency noise component [10, 33, 68]. In the FBP algorithm, radial filtering can be applied in the form of the window function (see Fig. 3.5) in presence of noise (since the ramp filter itself does not reduce noise). Usability of radial filtering can be determined from the projection theorem (Eq. 2.9). In contrast to radial filtering, angular filtering (i.e. filtering across the projections) of the sinogram data introduces tangentially non–uniform blurring to reconstructed images (see Fig. 5.1). Therefore, angular filtering of the data is generally avoided [13]. In some cases, however, angular filtering is performed through the application of a two dimensional filter. In addition, some improvements for angular filtering have been published [2, 74]. In the case of three

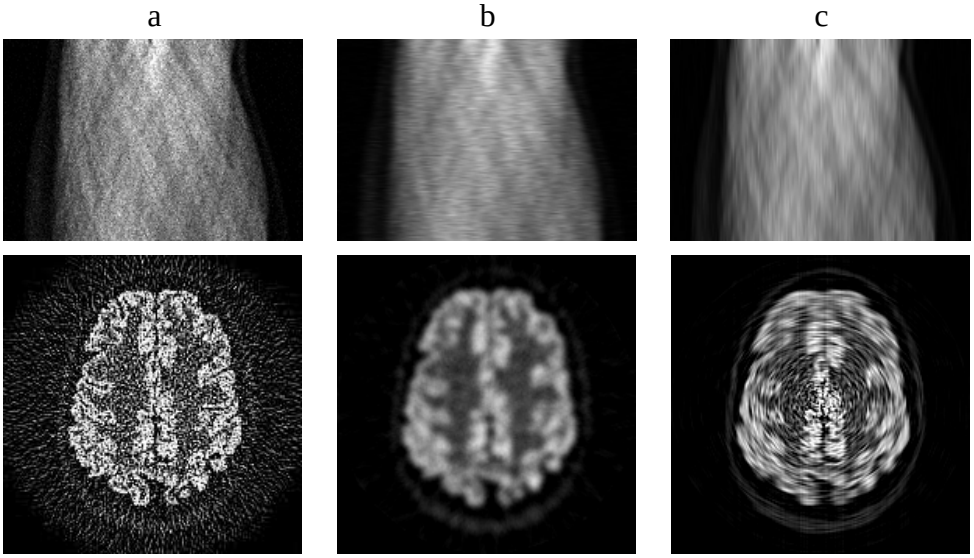

Figure 5.1: An illustration of the different sinogram filtering directions: a) the initial noisy sinogram and the reconstructed image; b) the sinogram after radial filtering and the corresponding reconstructed image; and c) the sinogram after angular filtering and its FBP–image. The different filtering directions can be seen in the sinograms due to the "stripes" along the corresponding directions. In c), notice the tangential blurring in the FBP–image. The employed filters were linear mean filters. The images share a common gray scale.

dimensional data, axial filtering of the sinograms (i.e. filtering across the two dimensional cross–sections) is also accepted method for filtering (e.g. [44]).

In the following Chapters 8 and 9, we consider sinogram data filtering employing different linear and non–linear filters in the sinogram and stackgram domains. Mainly, in our studies, we focus on effects of stackgram filtering along the angular direction, in comparison with the sinogram domain filtering. Fig. 5.1 expresses well the motivation for our studies, since filtering along the angular direction of the sinogram introduces clear tangential blurring.

Chapter 6

Compensation of Incomplete Sinogram Data

In limited angle tomography, incomplete range of angular views makes image reconstruction from the incomplete data difficult. In this chapter, first we review the problem of limited angle tomography, and then briefly go through some algorithms for the incomplete sinogram data. Again, the reason to present the algorithms or procedures is more like to give a general picture of the methods, and thereby provide a basis for using stackgrams for the limited angle problem.

6.1 Limited Angle Tomography

The projection theorem (Eq. 2.9) relies on the fact that a complete range of the line integral sets is available (at least) over $\theta \in [0\ \pi)$ for the inversion. All the projections are needed to reconstruct $f(x, y)$ accurately without artifacts. In limited angle tomography, however, the angular range of the projections is restricted, i.e. the Radon transform $\mathcal{R}$ (Eq. 2.3), and thus the stackgram h, is available only for a subset of $[0\ \pi)$. We denote this subset as $\phi \subset [0\ \pi)$, and the corresponding limited Radon transform operator as $\mathcal{R}_\phi$. Different limited angular ranges of the projections for ϕ are illustrated in Fig. 6.1. As regards the projection theorem, the unknown part of the angular range need to be recovered in order to obtain the full two dimensional spectrum of $f(x, y)$. This is an ill–posed problem, and actually "severely ill–posed" [53], depending on the missing range of ϕ.

The ill–posed limited angle problem is unsolvable without *a priori* information about the underlying object f [53]. If there is enough knowledge available in advance about the object, the problem or an inverse of $\mathcal{R}_\phi$ can be estimated.

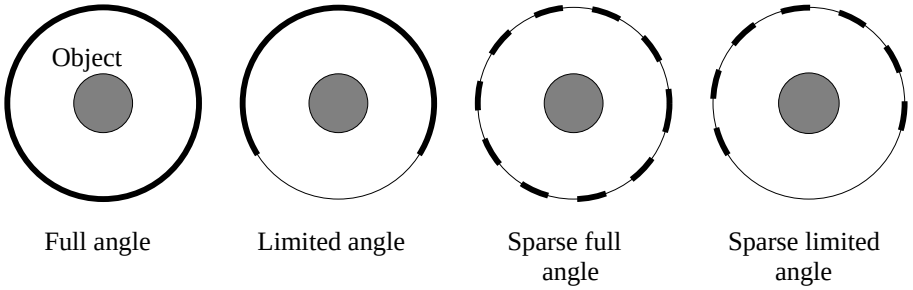

Figure 6.1: An illustration of four different types of the ranges for angular views: a) full range, b) limited range, c) sparse full range, and d) sparse limited range. The bold lines denote the available range of the line integral paths.

We do not review any stabilized inversions for the problem, but one can find such inversion formulas e.g. in the tutorial [57].

6.2 Algorithms for Incomplete Projection Data

In practice, there exist several limited angle imaging modalities or geometries, such as BPET [19], MDAPET [4], or X–ray applications [45]. Fig. 6.2(a) illustrates a sinogram of the classical limited range of views, while Fig. 6.2(b) shows an example of the limited range of the data in modern acquisition, such as in PENN–PET [35].

In limited angle tomography, there are two different approaches to recover the incomplete sinogram data: 1) the inversion for the limited view data can be modeled in the reconstruction algorithm, in order to obtain a reliable image; or 2) the missing part of the projection data can be compensated prior to the image reconstruction. The image reconstruction based algorithms can usually estimate the image from a narrow range of views better than the methods which compensate the missing range prior to reconstruction. In the next sections we describe in brief some approaches for solving the limited angle problem.

6.2.1 Image Reconstruction Based Algorithms

Statistical image reconstruction methods [31] are advantageous for the problems as limited angle tomography, since the imaging system can be modeled and *a priori* information about the data can be incorporated for reconstruction. Several algorithms for the problem have been published. For example in PET, statistical image reconstruction methods for limited PENN–PET data

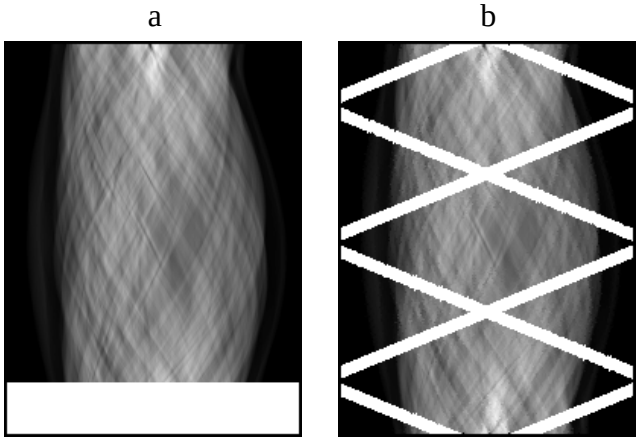

Figure 6.2: An illustration of two limited view sinograms: a) classical limited range of data; b) limited range of projections in PENN–PET acquisition.

have been introduced (see e.g. [38]). For limited X–ray tomography, statistical inversion methods are considered e.g. in Ref. [73]. Besides, different algebraic approaches for the problem have been published, one of the methods is based on the ridge functions [37].

The Fourier–based iterative algorithms (see e.g. [14]) provide another approach for the limited view problem. These algorithms do not employ the information about the imaging system as the statistical reconstruction algorithms, but convert the problem to spectral extrapolation via the projection theorem. The Fourier-based algorithms are generally faster than the statistical ones.

6.2.2 Extrapolation of Missing Sinogram Values

A different approach for the limited angle problem is to compensate the missing projections prior to image reconstruction, and then reconstruct the compensated sinogram with standard reconstruction algorithms such as FBP. The compensation of the missing values, or extrapolation along the angular direction, can be performed employing many different algorithms. A well known algorithm is the Gerchberg–Papoulis (GP) extrapolation method [61], which is an extension of the uniform sampling theorem to non-uniformly sampled data. Extrapolation algorithms for noisy data based on GP have also been studied [30]. Recently, an accelerated GP algorithm has been introduced as well [71]. A generalization of the GP method is denoted as Clark–Palmer–Lawrence (CPL) interpolation [11]. These GP based methods are usually applied along the angular direction

of the sinogram. Direct extrapolation along this direction, however, introduces non–uniform blurring in reconstructed images. This is the same effect as can be observed in angular sinogram filtering [13]. Thus, more sophisticated methods are needed.

One such methods utilizes the shape of the spectral support, since it is known that the spectral support of complete sinograms is bowtie–shaped [66]. This information is exploited in a linear and computationally efficient extrapolation technique [90], which is similar to the transform–based CPL, but exploits regularization based on the shape of the spectral support.

The Fourier–based iterative algorithm as well as CPL–based methods can be regarded as transform techniques that incorporate little *a priori* knowledge about the data. Another approach for sinogram extrapolation is based on a finite series expansion method, which can take into account *a priori* information as constraints. These kinds of algorithms are e.g. the affine transformation method of Reeds and Shepp (or the squashing method) [67], the method of projections onto convex sets (POCS) [72], or a method proposed for PENN–PET data [34]. The POCS method, as well as the method for PENN–PET acquisitions, estimates the sinogram iteratively (the methods do not reconstruct the image). A comparative study [59] for the CPL, squashing, and POCS methods concludes that POCS provides the best performance for the extrapolation techniques. The POCS method, however, is sensitive to noise amplification, therefore more stabilized solutions for the technique has been examined [28]. As regards the squashing method, the technique has been found to be identical to FBP (without any extrapolation of missing values) under certain assumptions [58]. Therefore, this affine transformation method is not necessarily applicable for the limited angle task.

In Chapters 8 and 9, we employ the GP method to evaluate the behavior of the extrapolation procedure in both the sinogram and stackgram domains. The GP method does not utilize *a priori* knowledge about the data, thus it provides fair comparisons between the two domains. In the thesis, we consider only the classical limited range of views as shown in Fig.6.2(a).

Chapter 7

Alignment of Tomographic Data

This chapter describes the object registration problem in medical imaging. Different procedures for image registration (or alignment) are reviewed, giving a short overview of some general principles for the registration task. However, the goal of this thesis is to provide a technique to align sinogram (or stackgram) data prior to image reconstruction. Thus, many of the algorithms to be presented in the chapter are not feasible for such a "sinogram data–driven" approach. Besides, there are not so many studies about sinogram based registration methods to be reviewed, especially for three dimensional data.

7.1 Image Registration

An image registration problem arises in many different tomographic modalities. According to Ref. [25], the term registration means "determining the spatial alignment between images of the same or different subjects, acquired with the same or different modalities, and also the registration of images with the coordinate system of a treatment device or tracked localizer". That is, in image registration, the problem is to find a suitable spatial transformation between two images, say $f_R(x, y)$ and $f_T(x, y)$, so that the images became similar to each other. The spatial correspondence of the images f_R and f_T is not known, but the objective of registration is to find such a transformation in a way or another. The transformation is solved usually in the image domain (x, y), not in the sinogram domain (l, θ).

In registration, one image is viewed as a reference, we denote this as f_R. The other image f_T is regarded as a deformable template. The problem is to find a transformation $\tau : \mathbb{R}^2 \rightarrow \mathbb{R}^2$ for the deformed template image f_D such

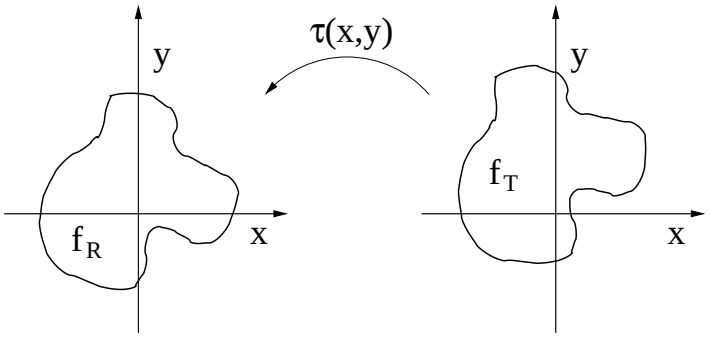

Figure 7.1: The reference image f_R at a certain (x, y) position, and the template image f_T at different coordinates. The problem in registration is to find the transformation $\tau(x, y)$. The figure illustrates a global rigid transformation, in which only global (x, y) translations and rotations are possible.

that it is similar to the reference image f_R. This can be formalized as [52]

$$f_D \triangleq \mathcal{D} f_T = f_T \circ \tau(x, y) = f_T(\tau(x, y)), \tag{7.1}$$

where $\mathcal{D}$ is the deformation operator.

The transformation τ can be 1) rigid, 2) affine, 3) projective, or 4) curved (or elastic). The rigid transformation allows only translations and rotations of the image coordinates (see Fig. 7.1). The affine transformation maps parallel lines onto parallel lines. The projective transformation maps lines onto lines, and the curved transformation maps lines on curves [49]. The curved transformation includes all the other transformations, likewise each of the four transformations is a special case of the ones described before it. Similarly, a combination of e.g. the affine and rigid transformations can be expressed by a single affine transformation. In the following chapters, we consider mainly the rigid transformation. A rigid transformation of the object image $f(x, y)$ transforms both the sinogram $g(l, \theta)$ and stackgram $h(x, y, \theta)$ coordinates as described in Table 4.1.

The different transformations can also be global or local. A global transformation applies to the entire image f, but a local transformation applies only to subsections of the image.

7.1.1 Extrinsic and Intrinsic Registration

Image based registration can be divided into two different bases, that are extrinsic and intrinsic methods [49]. Extrinsic methods are based on foreign objects,

which are attached to the object or the patient and designed to be clearly visible in the acquired images (e.g. stereotactic frame [79]). In extrinsic registration, the registration parameters can be often computed precisely, but the attached fiducials need to be inserted prior to the acquisition. The markers can also be uncomfortable for the patient, and the external fiducials often restrict to detect only rigid transformations. Intrinsic methods, on the other hand, exploit only the acquired image content without any external fiducials. Intrinsic registration, to be discussed next, can be further divided into three different approaches: landmark, segmentation, and voxel property based methods [49].

7.2 Image Registration Algorithms

In this section, we provide a short overview of different registration techniques. We are not considering the techniques very deeply, since the field of image registration is huge and includes many different modalities and procedures. Thorough surveys or reviews on image registration have been published, see e.g. [82, 49, 25].

This far, we have considered only two dimensional images. Image registration, however, is often applied for three dimensional data. In this thesis, a three dimensional image consisting of voxels is regarded as a stack of two dimensional images acquired from two dimensional cross–sections of the object.

We discuss only intrasubject registration, not intersubject registration [25] which would include e.g. registration of an object to an atlas (see e.g.[69]). Intrasubject registration concentrates on registration of images of the same object (patient) from the same or different imaging modalities. This includes also the one–to–one transformation. A registration problem such as this arises e.g. in PET–to–PET alignment, in which the data of equal dimensionality are acquired with the same imaging modality. The PET–to–PET alignment is required, for example, in list mode acquisition [83] or in multiple acquisition frame (MAF) method [64]. In the list mode, the data are acquired in short time frames, which are then realigned into a sinogram prior to the image reconstruction. In MAF, on the other hand, the short time frames are aligned after reconstruction and then combined (see Fig. 7.2).

7.2.1 Landmark Based Methods

Landmarks can be anatomical or geometrical [49]. Anatomical landmarks are accurately recognizable points in the images, whereas geometrical landmarks have more geometrical properties, such as corners. Landmark based regis-

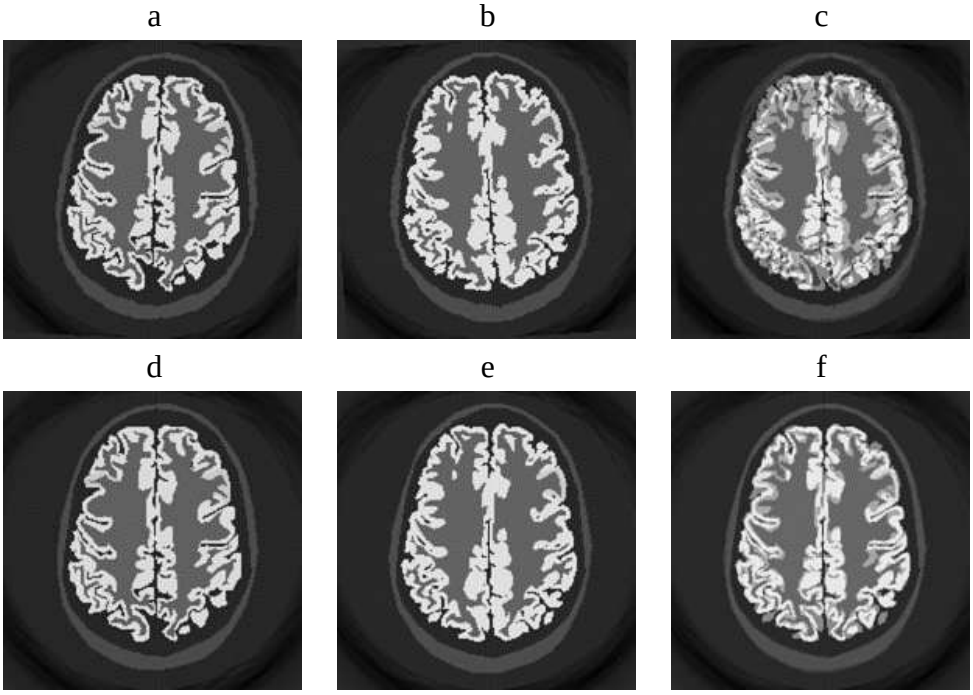

Figure 7.2: An illustration of the registration problem in one–to–one acquisition in PET (such as MAF). In a) and b), the object at time t_1 and t_2, respectively. Notice the different positions (and tracer distributions) of the images. In c), an average of the two images is clearly distorted. On the other hand, in d) and e), the images are aligned into the same position, although their distribution slightly differs (i.e. the registration problem is not exactly one–to–one). In f), the average image of the aligned images is visually much more informative compared to the image without alignment (c).

tration involves recognition of the corresponding points in the images to be aligned. The image transformation is determined based on the relations of the corresponding landmarks. Often, the set of the landmark points is much sparser than the initial image content. Because of that, the landmark based methods are often applied for registration of rigid or affine transformations. On the other hand, the sparse set of points enables the design of fast algorithms since all the image content is not needed for registration. Generally, the landmark based algorithms minimize the average distance, such as the Procrustean metric, between the landmark points (see e.g. [18]). A popular and well–known algorithm for this task is the iterative closest point (ICP) algorithm [6].

7.2.2 Segmentation Based Methods

Segmentation registration is based on the alignment of higher order segmented structures such as curves, surfaces, and volumes. Segmentation registration algorithms can be based on either rigid or a deformable model [49]. The rigid model based algorithms extract anatomically the same structures from the images and then align them as such. A well–known rigid model based method is the head–and–hat algorithm [63]. Deformable based registration procedures extract structures (surfaces, curves, and etc.) of one image and then elastically deform and fit the structures to the other image(s). Deformable models are often denoted as snakes or active contours in literature. The deformable methods are iterative, and they usually need a good initialization in order to converge. Such algorithms are e.g. non–rigid matching using "demons" [77] or a fully automatic surface extraction method [78].

7.2.3 Voxel Property Based Methods

Voxel based registration methods exploit the intensity values of voxels directly without any prior data reduction (i.e. sparse sets of landmarks or segmented structures). The voxel based methods can also be divided into two approaches [49]. First approach is to reduce the image gray value content to represent only e.g. orientations. The second approach is to utilize the whole image data content as such for registration. Principal–axes based methods are typical examples of reductive voxel based registration methods. In these methods, the center of gravity and its principal–axes are calculated, and then the registration is performed based on alignment of the evaluated center and orientations (e.g. [5]). Voxel property based methods using the full image content are theoretically the most flexible registration methods, since they do not reduce the image data prior to the registration process, but use all the available information [49]. There exist several different approaches for voxel property based methods, such as cross–correlation, minimization of variance of intensity ratios (e.g. [48]), maximization of mutual entropy (e.g. [47]), and minimization of the absolute squared intensity differences (e.g. [80]). One of the algorithms is the well–known automated image registration (AIR) method [84], based on minimization of variance of intensity ratios. We concentrate in the following chapters only on the approach of minimizing intensity differences, which has been shown to be optimal for similar images.

7.3 Registration in Sinogram Domain

All the above mentioned registration techniques employ usually reconstructed images for registration or alignment. Another approach would be to use sinogram data, in which, however, even local motion of the object introduces global shifts (see Table. 4.1) explaining why the sinogram data are not used so much for registration. On the other hand, it would advantageous to use directly the measured sinogram data for registration in order to avoid errors or artifacts introduced by the ill–posed image reconstruction process. Some studies on motion correction in the sinogram domain have been published (e.g. [46, 76]). These methods, however, are usually for two dimensional data, and therefore they are not so suitable e.g. for modern PET studies. Besides, motion correction (or alignment) is almost impossible to perform reliably without re–projections (i.e. the Radon transform of a reconstructed image) in the sinogram domain. The re–projections are more blurred than the initial projections making the registration more difficult. An algorithm for motion correction of three dimensional data using re–projections has been studied in Ref. [26].

In Chapters 8 and 9, we discuss registration or alignment based on intensity values of the locus–signals in the stackgram domain resulting in aligned sinograms. Instead of voxels, the difference of the intensity values of the locus–signals is minimized. This method can be regarded as voxel based minimization of the absolute squared intensity differences. We consider this as “locally rigid” PET–to–PET intrinsic registration.

Chapter 8

Methods and Results

In this chapter we go through the methods and the results of the thesis consisting of the attached publications [P-1, P-2, P-3, P-4, and P-5]. The first section considers filtering in the stackgram domain [P-1, P-2, and P-3]. The findings of the filtering studies gave also the motivation for extrapolation of stackgram data for limited angle tomography [P-4], which is discussed in the second section. In the last part of the chapter, we present methods and results for alignment of tomographic data in the stackgram domain [P-5]. The main emphasis of the last section is in the one–to–one alignment.

We do not present the same image data as in the publications, but the shown example images are created from the Zubal phantom (shown in the previous chapters as examples) and only stackgram processed data are presented, although we present for comparison some quantitative evaluations of different methods. Deeper comparative studies can be found in the attached publications.

8.1 Filtering in Stackgram Domain

A proper noise reduction is an important problem especially in emission tomography. The stackgrams provide a new approach for the problem. The stackgram domain has been originally developed for sinogram data filtering [P-1] to offer a filtering environment for the signals along the sinusoidal trajectories of the sinogram in such a manner that the signals could be filtered separately without interfering with the neighboring signals. That is, the angular direction of the data could be exploited in a more convenient way. As we describe in the previous chapter, the angular θ direction of the sinograms is not usually exploited in sinogram data filtering, whereas the radial l direction is commonly applied for noise reduction (see the directions in Fig. 3.1).

Resolution of the reconstructed image is proportional to smoothing or a resolution loss introduced by a radial filter, according to the projection theorem. In a discrete stackgram $\mathbf{h}(x_i, y_j, \theta_m)$, filtering of each locus–signal along the angular θ axis should not cause resolution loss (in an ideal case) in the spatial (x, y) direction, since one dimensional filtering does not intersect the spatial coordinates of the different locus–signals. In practice, however, this is not the case, but means that when filtered stackgrams are transformed back to the sinograms, the spatial resolution loss of the reconstructed images has different meaning or appearance, compared to the sinogram domain filtering due the different filtering direction. Technically, filtering in the stackgram domain without spatial resolution loss (in its standard meaning) could be achieved if the stackgrams are summed up, and reconstructed to images e.g. with the rho–filtered layergram method. In the case of image reconstruction from the stackgrams, however, filtering along the locus–signals would have very little effect for noise reduction in the reconstructed image. This is due the fact that the average values of the locus–signals correspond to the intensity values of the image, and the filters often preserve the average of the filtered signals. Thus, the intensity values of the image pixels (and noise) would remain the same regardless of stackgram filtering. This, again, is not a problem when the filtered stackgrams are transformed back to the sinograms, because then the filtered signals are not summed up along the θ axis.

The results for the filtering studies can be found in [P-2 and P-3]. The first experimental study [P-2] investigates filtering of noise in the radial and angular sinogram directions (including two dimensional filters) in comparison with the angular stackgram direction. In addition, the reversible discrete stack operator (Eq. 4.9 and 4.11) was introduced in [P-2]. This reversible implementation has been applied in all the studies. In [P-2], three different numerical phantoms were used to evaluate the different methods in the study. We performed hundred noise realizations with ten different noise levels for the data. We employed finite impulse response (FIR) filters [27] with Gaussian kernels of ten different FWHM values to compare the different filtering directions in the study. Since the filtering directions have different meaning in each case (as regards FWHM or resolution loss), the results were compared at a certain resolution. According to the quantitative results, radial filtering provides the best resolution versus noise trade–off for the compared methods. Similarly as in the case of radial filtering, geometrical distortions or non–uniform blurring cannot be observed in angular stackgram domain filtering, unlike in angular sinogram filtering. Besides, the noise component in the FBP–images after stackgram filtering seems to be less disturbing[1]. Stackgram filtering clearly preserves the sinusoidal struc-

[1]By "the less disturbing noise component" we mean that the noise in the reconstructed

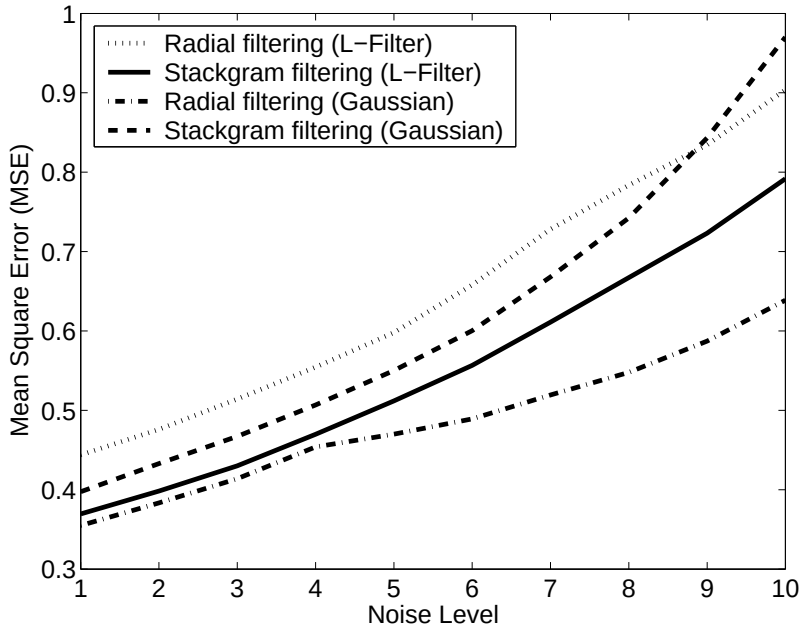

Figure 8.1: Radial sinogram filtering versus angular stackgram filtering. The curves are combined from the studies [P-2] and [P-3]. The kernel weights of the filters are not fixed in the shown curves (see details in the publications), but the best MSE values over the noise levels are shown regardless of the filter weights. At the low noise levels, stackgram filtering with the L–filters performs quantitatively almost as well as radial sinogram filtering with the Gaussian filters. Stackgram filtering seems to perform better with the non–linear filters, whereas radial sinogram filtering performs better with the linear filters.

tures of the filtered sinograms. One important finding of the study [P-2] is also that the required FWHM value of the filters at the matched resolution in stackgram filtering is more than two times wider than in radial filtering.

In the filtering study [P-3], we used the same data, procedure, and evaluations as in [P-2] to compare the radial sinogram and angular stackgram filtering methods, with one exception. The exception was the selection of the filters. Instead of using linear filters for noise reduction, we employed non–linear L–filters [3] for the study. Each output point of the L–filters is obtained as a weighted sum of ordered data values in the moving window. Let $\mathbf{a}$ be the weight vector and $\mathbf{x} = [x_1, x_2, \ldots, x_N]$ the input values. The L–filter can be

images after stackgram filtering looks usually more "powdery", in comparison with radial sinogram filtering.

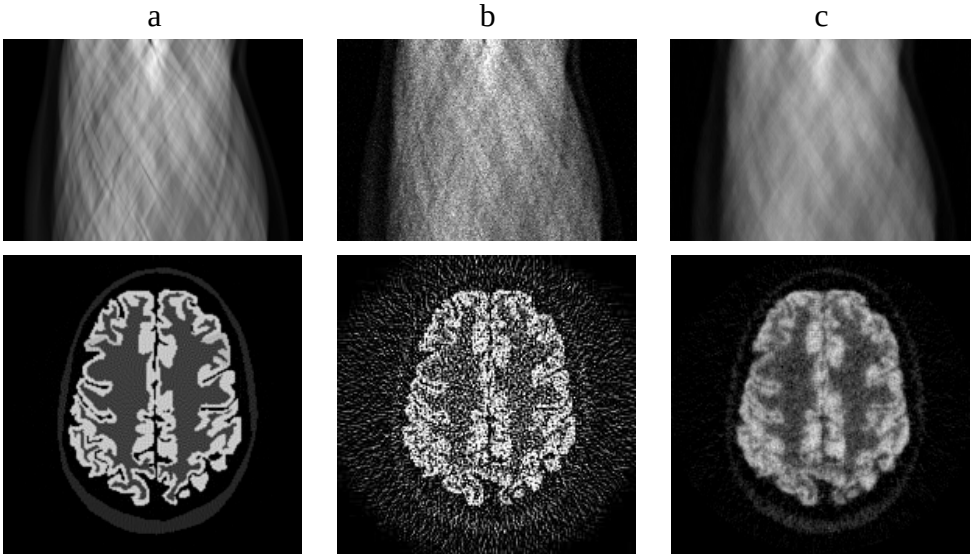

Figure 8.2: The Zubal phantom data: a) an upper part of a noiseless sinogram and the corresponding FBP–reconstructed image; b) a noisy sinogram and its FBP–image; c) a stackgram filtered sinogram and the reconstructed image. The employed filter was a non–linear L–filter with Gaussian weights (FWHM 3.41 elements). As it can be observed (c), the sinusoidal structure of the sinogram is preserved after stackgram filtering (compare to the sinograms in Fig. 5.1). The details of the FBP–image after stackgram filtering are also preserved well. The images share a common gray scale.

defined as $L(\mathbf{x};\mathbf{a}) = \sum_{i=i}^{N} a_i x_{(i)}$, where $x_{(i)}$ denotes ordered input points. We applied ten different Gaussian weights for the L–filters. In the study [P-3], similar effects can be noticed as in [P-2], but in the case of [P-3] the stackgram filtering method seems to perform better than radial filtering. The resolution versus noise trade–off is advantageous for stackgram filtering.

The best mean square errors[2] (MSEs) versus noise levels over the different filter kernels of the studies [P-2] and [P-3] are shown in Fig. 8.1. As can be observed, radial filtering with the Gaussian filters performs better than angular stackgram filtering, although the difference is small when the noise levels are low and stackgram filtering is employed with the L–filters. As regards the curves in Fig. 8.1, the non–linear filters seem to be more suitable for stackgram

[2]In this thesis, the mean square error is defined as $1/n \sum_{k=1}^{n}(x_k - y_k)^2$. Similarly, the mean absolute error can be written as $1/n \sum_{k=1}^{n} |x_k - y_k|$. These definitions are slightly different than in statistics.

filtering, whereas radial filtering performs better with the linear filters. Fig. 8.2 shows the typical behavior of stackgram domain filtering (using an L–filter of length 11). The sinusoidal structure of the sinogram is clearly preserved and the noise structure of the reconstructed image is not disturbing.

8.2 Extrapolation in Stackgram Domain

The problem of reconstructing an image from limited view data is a "severely ill–posed" problem, as mentioned previously. This makes the reconstruction problem more difficult than in the case of full view data. In this thesis, we extrapolate the missing sinogram values in order to use common algorithms for image reconstruction. According to our experimental filtering studies, the angular direction in the stackgram domain, unlike in the sinogram domain, can be exploited without causing non–uniform blurring to the reconstructed images. This gives also the motivation for extrapolation of the missing data values for limited angle tomography, since extrapolation of a signal can be seen as a filtering task (in the deterministic sense). Thus, the findings of [P-2] and [P-3] can suggest that extrapolation (as well as filtering) in the stackgram domain provides better results compared to angular extrapolation (or filtering) of the sinograms.

We compared extrapolation of missing data values in both sinogram and stackgram domains along the angular directions in [P-4]. Numerical noiseless data and four different ranges (from 157° to 174°) of limited views were used. The GP extrapolation method was applied in the form of an extrapolation matrix [70]. The extrapolation technique can be seen as a sinusoidal fitting of signals. The missing values of signals to be extrapolated are filled by the values of a best matched curve consisting of different sinusoidal signals of different frequencies. The amount of frequencies in the extrapolated signals is controlled by a cut–off frequency. The extrapolation method is iterative by its nature and the signals need to be band–limited. Worth noticing is that the extrapolation procedure is sensitive (or unstable) if the cut–off frequency is (relatively) high (e.g. 0.15) or the range of the missing values is considerable. Thus, extrapolated signals can contain significant errors or artifacts, if the initial signals consisted of a wide range of frequencies. In the study [P-4], we applied 30 different cut–off frequencies for the four limited range of views to study the behavior of the sinogram and stackgram domain extrapolation procedures. This means that the extrapolated parts of the signals could maximally consist of curves of 30 different frequencies (plus the DC component). The sinograms $\mathbf{g}(l_n, \theta_m)$ and the stackgrams $\mathbf{h}(x_i, y_j, \theta_m)$ were extrapolated along the angular θ direction. The

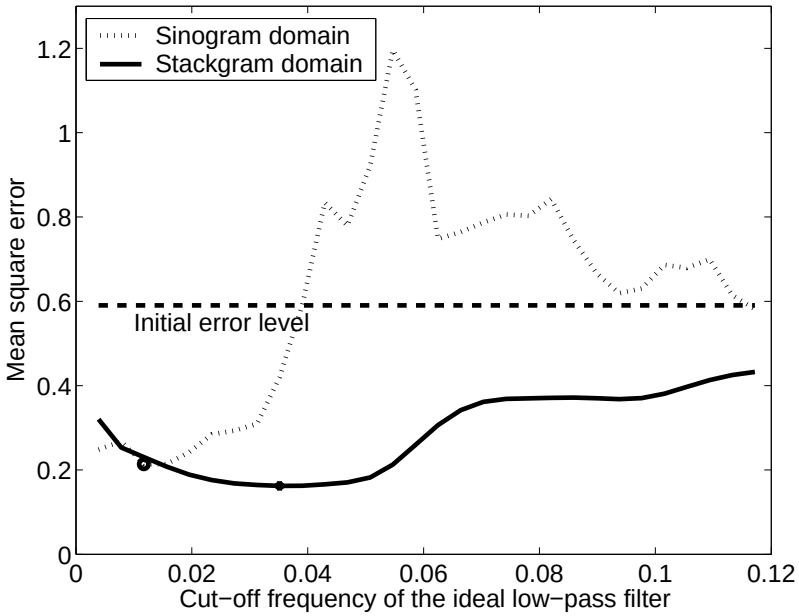

Figure 8.3: MSE of the reconstructed images versus the cut–off frequency of the extrapolator (Nyqvist 0.5). The initial error level represents the MSE error without any extrapolation. The missing range of the projections were 17° (or 9.5% of the full range). Extrapolation in the stackgram domain provides better results in the MSE sense and seems to perform in a more predictable way than sinogram extrapolation. The marked dots emphasize the minimum MSE values in both cases. In the minimum MSE points, stackgram extrapolation provides more complex extrapolated signals, since the cut–off frequency of the extrapolator is higher compared to the corresponding sinogram extrapolator. The curves consist of 30 samples. See also [P-4].

length M of the signals or the number of views was 257. The aim of the study was to compare the different domains for extrapolation, not to provide ready to use results.

Fig. 8.3 shows the MSE versus the cut–off frequency of the extrapolation matrix for angular extrapolation in the sinogram and stackgram domains [P-4]. As can be seen, stackgram extrapolation seems to be more robust than sinogram extrapolation in the MSE sense. Besides, the cut–off frequency in the minimum MSE points for stackgram extrapolation is higher and therefore can provide more complex extrapolated signals, although the cut–off frequency is relatively low due to the sensitive extrapolation procedure. Angular extrapolation introduces tangential non–uniform blurring in reconstructed images [P-4],

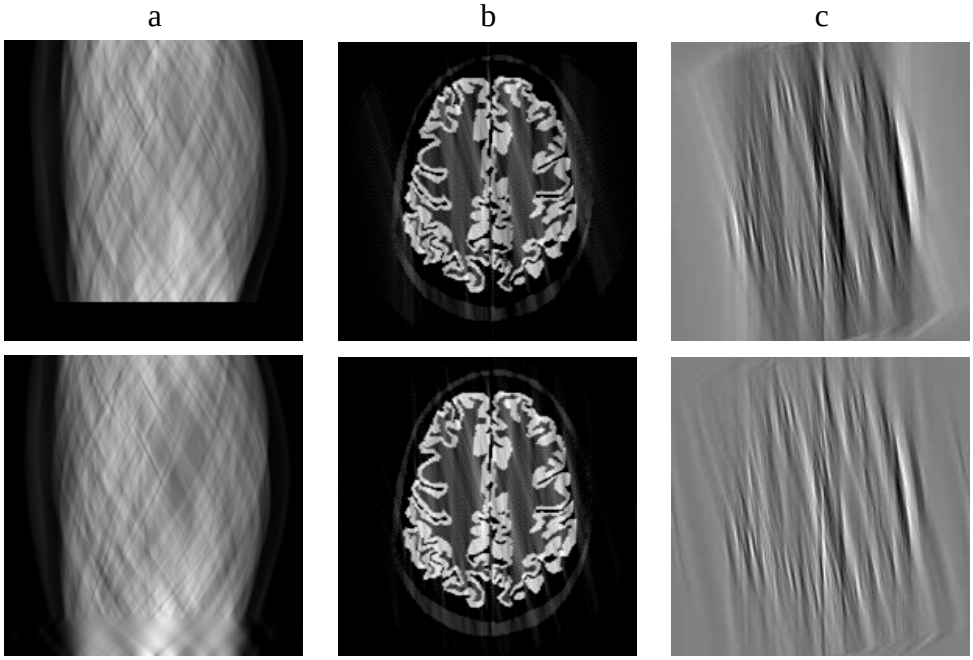

Figure 8.4: Stackgram extrapolated results. Upper row: a) lower part of limited view sinogram; b) "naive" FBP–reconstruction; and c) an error image compared to the FBP–image from the full view sinogram. Lower row: the corresponding results after stackgram extrapolation. The missing range of the projections were 17° or 25 projections. The reconstructed images contain artifacts and look rather similar. However, the error image after stackgram extrapolation (lower row in c) contains observably less variations than the initial error (upper row in c).

similarly as in the case of angular filtering [13]. These findings are consistent with our filtering studies [P-2] as well. Typical results after "naive" FBP–reconstruction[3] and stackgram extrapolation are shown in Fig. 8.4. As expected, the extrapolated sinogram (Fig. 8.4(a)) consists of sinusoidal signals, unlike in the case of angular sinogram extrapolation [P-4]. The shown reconstructed images (Fig. 8.4(b)) look almost equal. The differences can be seen better in the error images (Fig. 8.4(c)). The tangential distortions cannot be observed in the FBP–image after stackgram extrapolation, unlike in the case of angular sinogram extrapolation [P-4].

[3]In "naive" reconstruction, the missing projection values are simply replaced by zeros.

8.3 One–to–One Alignment in Stackgram Domain

The previous two stackgram applications (filtering and extrapolation) are very different than the one–to–one alignment technique to be described next. The algorithm is designed for sinogram data having time frames. That is, short time frames need to be aligned for a reference frame. Similar data are acquired e.g. in PET list mode acquisitions. In the list mode, acquired data are realigned before binning into sinograms, prior to image reconstruction. Only a few alignment algorithms for sinogram data have been published, as mentioned in the previous chapter. The alignment or registration is commonly performed in the image domain. Moreover, the proposed alignment algorithms based on sinogram data are usually feasible only for two dimensional data. In other words, the sinograms from different cross–sections of the object cannot be aligned. The acquisitions, however, are three dimensional and therefore the sinograms of the different cross–sections should be aligned.

In this thesis, we are not considering truly three dimensional sinograms (or planograms). We consider a three dimensional image as a stack of two dimensional images reconstructed from a stack of sinograms. That is, let $\mathbf{G}(l_n, \theta_m, z_k) = [\mathbf{g}_1(l_n, \theta_m), \mathbf{g}_2(l_n, \theta_m), \ldots, \mathbf{g}_K(l_n, \theta_m)]$ be the stack of sinograms (or "pseudo three dimensional" sinogram). In which case the three dimensional image $\mathbf{F}(x_i, y_j, z_k) = [\mathbf{f}_1(x_i, y_j), \ldots, \mathbf{f}_K(x_i, y_j)]$ can be reconstructed from the sinograms of the cross–sections or planes of $k = 1, 2, \ldots, K$. Under certain assumptions, the "pseudo three dimensional" sinograms acquired at different times, say $\mathbf{G}_R$ and $\mathbf{G}_T$, can be aligned without image reconstruction in the stackgram domain, unlike in the sinogram domain [P-5].

The algorithm [P-5] is based on comparisons of the locus–signals in their three dimensional local neighborhood. Let $\mathbf{H}_R(x_i, y_j, z_k, \theta_m) = [\mathbf{h}_1(x_i, y_j, \theta_m), \ldots, \mathbf{h}_K(x_i, y_j, \theta_m)]$ be a reference stack of stackgrams and $\mathbf{H}_T$ a template stack of stackgrams from the reference $\mathbf{G}_R$ and template $\mathbf{G}_T$ sinograms, respectively. Notice that the locus–signals $\mathbf{h}(\theta_m)$ are at each (x_i, y_j, z_k) position and form the fourth dimension. The reference data $\mathbf{H}_R$ and the template data $\mathbf{H}_T$ are assumed to be nearly equal (and "locally rigid"), since otherwise the comparison of the locus–signals would be difficult (see the properties of stackgrams in Table. 4.1). The alignment is performed in such a manner that for each reference coordinate $(x_i, y_j, z_k)_R$ the best matched locus–signal is moved from the corresponding neighborhood of the template coordinate $(x_i, y_j, z_k)_T$ to the right position, according to a similarity measure. In our study [P-5], we employed the MSE and the mean absolute error (MAE) as the similarity measures. Both the MAE and MSE measure similarities of the data based on intensity values. The MAE was mainly used in noiseless cases, whereas the MSE was

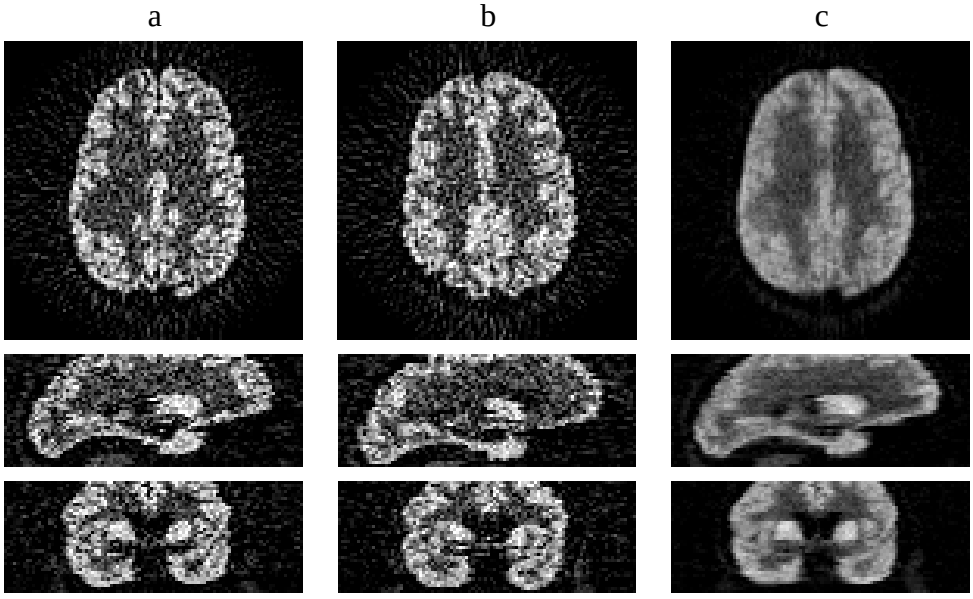

Figure 8.5: PET–to–PET alignment: a) The reference image; b) the template image; and c) the reconstructed image after stackgram alignment. The alignment performs accurately, although the aligned image is clearly blurred. This is due to averaging by the inverse stack operator after rearrangements of the locus–signals during the alignment procedure. All the images were reconstructed with the FBP algorithm. The images share a common gray scale. See also the error images in Fig. 8.6.

used for noisy data alignment. The MSE is more suitable for noisy data than the MAE. After the local alignment, the resulting aligned stack of stackgrams is transformed back to a stack of sinograms (this is denoted as the Method 1 in [P-5]). On the other hand, the aligned stackgrams can be reconstructed to images with the rho–filtered layergram method directly from the stackgrams (the Method 2). The method 2 is suitable for MAF like acquisitions. Technically, we did not use the rho–filtered layergram method in [P-5], but the sinograms were multiplied by the ramp filter prior to the stackgram transformations, and after the alignment the stackgrams were summed up to FBP–images (see the details of the algorithm in [P-5]). This, however, does not necessarily provide as accurate results as the rho–filtered method in presence of noise, since the ramp filter amplifies the noise component and makes the alignment more difficult. Therefore, the rho–filtered layergram method could be a more preferable implementation for the alignment, if the images are reconstructed from the

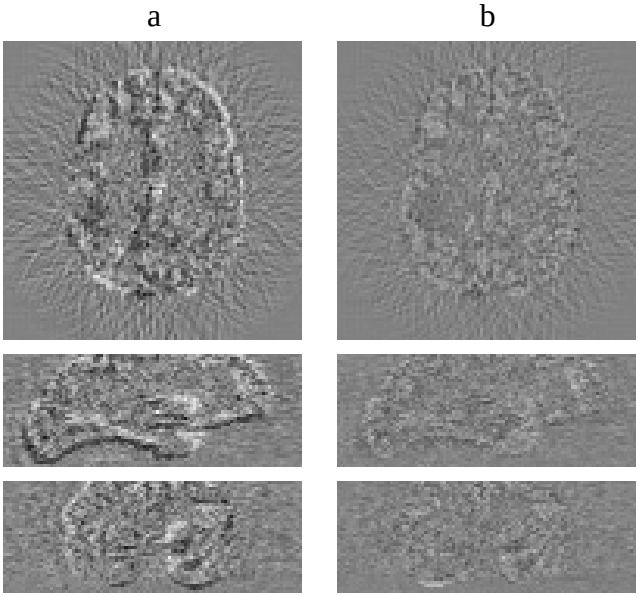

Figure 8.6: The error images: a) the reference compared to the template; and b) the reference compared to the aligned image. The alignment seems to perform accurately, although blurring of the image data can be observed. The images share a common gray scale.

stackgrams, although the two dimensional rho–filtering can introduce artifacts after the alignment process as well. Due to rearrangements of the locus–vectors in the Method 2, the voxels of the "stackgram reconstructed" images can be (fairly) independent of other voxels. In this study, we demonstrate the Method 2 with noiseless data using ramp filtering prior to the stackgram transformation, similarly as in [P-5].

Fig. 8.5, Fig. 8.6, and Fig. 8.7 show example results of the alignment with the MSE measure. Fig. 8.5 shows the reference and template images as well as the image reconstructed from the aligned sinograms (Method 1). The corresponding error images are shown in Fig. 8.6. The noiseless image in Fig. 8.7(b) is reconstructed directly from the stackgram (Method 2). The noiseless data were chosen due to the fact that the implementation of the Method 2 (i.e. ramp filtering prior to the stackgram transformation) makes the alignment difficult with noisy data. The alignment performs well in both cases (Method 1 and 2). However, there are clear differences between the two methods. That is, the Method 1 (Fig. 8.5) seems to introduce blurring more than the Method 2 (Fig. 8.7). An explanation for the blurring is averaging after the alignment into

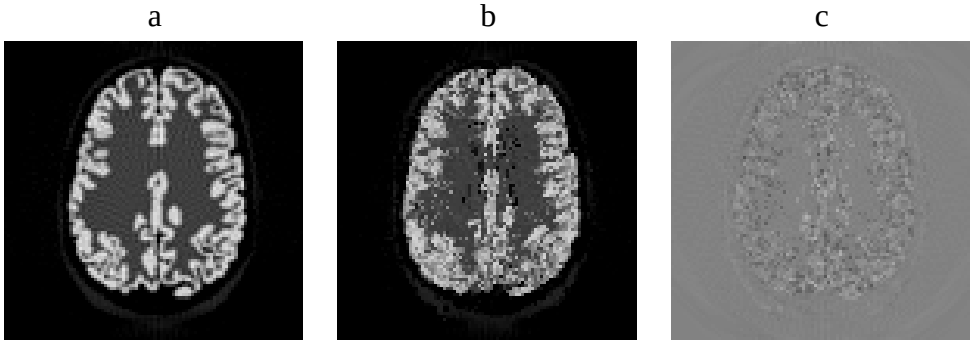

Figure 8.7: PET–to–PET alignment: a) The reference image; b) the aligned image reconstructed from the stackgram (Method 2); and c) the error image. The data are the same as show in Fig. 8.5, but without noise. The alignment performs well and the similar blurring effect as in Fig. 8.5 cannot be observed, but blurring is replaced by the "salt and pepper" like noise.

the sinogram projections from the stackgram layers (see the inverse stack operator Eq. 4.11). In the Method 2, there is no such averaging and therefore the "salt and pepper"[4] like noise structure of the aligned image can be observed.

In the study [P-5], we applied the alignment algorithm also for "locally rigid" data. That is, some structures of the object are moved while the rest of the object is stationary. See the chest phantom figures in [P-5] as examples. Data involving "locally rigid" transformations require alignment (or strictly speaking deformations) only for certain regions of the data.

[4]The "salt and pepper" noise is commonly referred to as intensity spikes or speckle. The intensity values of the corrupted pixels are near the maximum value (which looks like salt in the image), or alternatively near the minimum value (which looks like pepper).

Chapter 9

Discussion

We discuss the stackgram approach and its advantages and drawbacks in the presented applications in this chapter. All the ideas or thoughts to be discussed are not necessarily reported in the attached publications. One has to remember that the reported stackgram approach is a new concept and there are still many stackgram related things to be explored. The aim of the thesis has been mainly to study the behavior of the novel approach in the different applications. In this chapter, stackgram related implementation issues are considered before the applications: filtering, extrapolation, and alignment. Finally, some concluding remarks about the work are considered.

9.1 Author's Contribution to Publications

Publication [P-1] is the first scientific article of the stackgram domain approach for sinogram data processing. As the first author in [P-1], A. P. Happonen suggested the idea of filtering the signals along the sinusoidal trajectories of sinogram to S. Alenius, who then invented the stackgram concept. A. P. Happonen had an important role in developing the discrete stackgram implementation and designing the reported tests. Publication [P-1] was written in tandem with the both authors.

Publication [P-2] includes more precise definitions of the stackgram related operators in the continuous and discrete cases. Furthermore, more thorough and quantitative experimental tests of the new method are presented for wider scientific audience. In [P-2], A. P. Happonen had a significant role in designing and writing the paper, and performing the tests. The anonymous IEEE-TMI reviewers of the paper [P-2] gave also valuable advice and suggestions.

Publication [P-3] continues the article [P-2] by employing non–linear filters, instead of linear ones, for the study. A. P. Happonen designed and performed

the tests, and wrote the article as well.

Publication [P-4] presents an approach to employ the stackgram domain for extrapolation of missing data in limited angle tomography. A. P. Happonen designed the procedure and the experimental tests, and also wrote the article.

Publication [P-5] presents an alignment algorithm for tomographic data using the stackgrams. U. Ruotsalainen, the second author in [P-5], suggested the feasibility of performing alignment in the stackgram domain. A. P. Happonen designed and tested the reported algorithm. A. P. Happonen had a significant role in writing the article.

9.2 Implementation of Stackgram

In this thesis we present a reversible implementation for the transformation from the sinogram to stackgram domain using the three–pass rotation algorithm with sinc–interpolation. In our studies (especially in the filtering tests), it has been important to use the reversible transformation to cancel out the blurring effect introduced by poor or non–reversible interpolators [91]. The reversible implementation has enabled to examine the filtering effect in the stackgram domain without interfering with the blurring caused by interpolation. However, although sinc–interpolation provides the reversible implementation and accurate interpolation results, sophisticated spline interpolators (e.g. [21]) could offer better options for the implementation in the end. The stackgram implementation using spline interpolation would (perhaps) represent the true locus–signal values better, because of lack of the ringing effect by sinc–interpolation. Besides, it would not be necessary to implement the sinogram to stackgram transformation using image rotations as we have done, another possible choice would be a "direct" implementation of Eq. 4.1.

In our studies, the difference of the sampling rate (or resolution) of the locus–signals at different spatial positions was not discussed. The resolution of the locus–signals near the origin is more dense than near the borders (see Fig. 4.4). This fact could introduce non–uniform spatial blurring in the reconstructed images, when a fixed operator is employed in the stackgram domain. However, in our filtering and extrapolation studies, non–uniform blurring is not (at least) observable. Still, the difference in the sampling rate of the signals would need deeper investigations.

Worth noticing is also the data processing times for the three dimensional stackgram data in comparison with the two dimensional sinogram data. In the radial sinogram processing, the number of signals to be processed is M, when the length of the signals is N. In the angular sinogram processing, this is oppo-

site as N signals with the length of M. In the stackgram domain, however, the number of signals to be processed is $\frac{\pi}{4}N^2$ and the length of the signals is M. This means considerably longer processing times and more memory requirements for the data.

9.3 Filtering

The aim of the experimental filtering studies [P-2, P-3] has been to investigate the different filtering directions. We have been interested especially in the angular stackgram direction compared to radial sinogram direction. We have not tried to find a best possible choice for e.g. PET data filtering (i.e. using *a priori* information), although some studies have been performed already [41]. As regards the publications [P-2, P-3], stackgram filtering seems to perform better with non–linear filters compared to linear ones (Fig. 8.1). On the other hand, filtering with linear filters along the radial sinogram direction provides more quantitative results compared to non–linear stackgram filtering. The difference, however, is rather small when the noise level is low. An explanation for the advantage of using non–linear filters in stackgram filtering is in the redundant structure of stackgrams. In stackgram filtering, it is even more important to preserve high spatial differences (such as edges), compared to e.g. radial sinogram filtering, since after the filtering the layers of the stackgrams are averaged (which has the same effect as a low–pass filter) back to the projections of the sinograms. This causes extra spatial blurring. This blurring effect caused by the discrete inverse stack operator could be reduced by using a "non–linear" average (such as the L–filter) in the inverse operator. This kind of an "L–filter type" inverse stack operator would order the layers of the stackgram prior to the weighting and summing into the sinogram projections, whereas the inverse stack operator only averages the layers (see $\mathbf{w}$ in Eq. 4.11). This non–linear inverse stack operator could be suitable also in other stackgram applications.

Stackgram filtering does not seem to introduce non–uniform blurring in the reconstructed images, according to our studies. The angular information of the sinogram data can be exploited in a better way in the stackgram domain than in the sinogram domain. In addition, angular stackgram filtering seems to provide a less disturbing noise structure of the reconstructed images in comparison with sinogram domain filtering. In the studies, we reconstructed the images with the FBP algorithm, since it is linear and then the effect of filtering can be examined reliably. However, the "pleasant" or "natural" noise structure introduced by stackgram filtering could suggest that statistical reconstruction algorithms such as the MLEM method may exploit the data, resulting in better images. If

MLEM reconstruction with PET data was used after stackgram filtering, the different noise structure would require e.g. the NEC scaling [54].

The filtering region (which can be regarded as FOV) plays an important role in stackgram filtering (the region is denoted as $\mathbf{O}$ in Eq. 4.11). The same region is applied to process the signals in the other stackgram applications as well. Basically, this region should be equal to the boundary of the object, since the locus–signals outside the object do not contain any new information for the filtering. All the signals forming the background, not the object, could be omitted in stackgram filtering. This, however, is not that straightforward because the spatial region (or FOV) needs to be larger than the object in order to get a reliable filtered sinogram from the stackgram. If the filtering region (or the number of spatial samples of the stackgram layers forming the sinogram projections after stackgram filtering and the inverse stack operator) is too small, non–uniform blurring can be introduced to the reconstructed images.

9.4 Extrapolation

We compared the different domains for extrapolation using the GP method in [P-4]. According to our experimental tests, extrapolation of the missing sinogram values in the stackgram domain can be performed without introducing tangentially varying blurring, in contrast to angular sinogram extrapolation. This observation is consistent with our filtering studies. Besides, the stackgram domain seems to provide a more robust environment than the sinogram domain for extrapolation with the GP method.

The GP method provides a deterministic approach for extrapolation of limited view sinograms. Noiseless data with rather small ranges of limited views were employed in our study. A considerable limited range of views along with noise can make the GP method insufficient for real data.

The GP technique is based on extrapolation using the Fourier transform, which assumes the data to be periodic. This might partially explain the superiority of the stackgram based extrapolation, since the locus–signals are periodic in θ with period π, unlike the angular sinogram signals (see Table 4.1). In the study, however, we did not exploit any *a priori* information about the data. In extrapolation, *a priori* knowledge about the data would be crucial to obtain better results, since extrapolation is a “severely” ill–posed problem.

9.5 Alignment

We have proposed a simple alignment algorithm suitable for PET–to–PET registration based on local comparisons of the locus–signals [P-5]. Recently, the algorithm has been applied for lung PET imaging [65] to align lung tumors. Furthermore, effects of different filters for noise reduction prior to the alignment were studied in Ref. [40]. The purpose of the proposed algorithm is to offer an automated data–driven alignment technique for three dimensional PET data. Ref. [26] describes an algorithm with the same motivation. The algorithm [P-5] can be implemented to be fully automatic and it can (under certain assumptions, described below) align small local changes in three dimensional data. The resulting data can be aligned to sinograms (Method 1) or FBP (like) images (Method 2). Worth noticing is that in the Method 2, three–pass rotation with sinc–interpolation is not employed, since the transformation does not have to be reversible. Recently, an image reconstruction method having similarities with the "stackgram–reconstruction" (of the Method 2) has been presented in Ref. [9][1].

The measures we have applied for the similarity comparisons for alignment were the MAE and the MSE. In the alignment algorithm, various similarity measures could be used, the applied MAE and MSE measures were more like to demonstrate the performance of the algorithm than to provide an optimal solution for the similarity measure used in the algorithm. *A priori* information depending on the applied data would be needed to design the "optimal" similarity measure. However, it is not presumable that different similarity measures would improve the results significantly.

In the proposed algorithm, the data to be aligned are assumed to be nearly equal. This is due the fact that an (x, y) rotation of the object results in translations in the locus–signals along the θ direction (see Table 4.1). Besides, local translations or intensity differences introduce local translations or differences in the locus–signals to be compared. If the above mentioned deformations are too wide, the algorithm we have presented cannot compare the locus–signals reliably. A more advanced alignment algorithm which would take into account these deformations would naturally improve the results.

In principle, the proposed (simple) alignment algorithm can accurately align data only for spatial translations. Other deformations cannot be handled properly with the algorithm, as stated. However, we have assumed that the data to be aligned are nearly equal and involve "locally rigid" transformations (such as the chest phantom in [P-5]). According to the studies, the proposed algorithm can align such data without causing significant artifacts. Worth noticing

[1]The stackgram approach has been mentioned and cited in the article.

is also that the proposed algorithm performs more accurately for data having simple structures (compare Fig. 8.5 and 8.7 to figures in [P-5]). These simpler phantoms (as in [P-5]) represent better conventional PET data.

The effect of three dimensional motion is not so obvious in the case of stackgrams, since the data we have used are two dimensional cross–sections of the three dimensional object. In the stackgrams, there is lack of information about the truly three dimensional nature of the data, although this lack of information is not so significant as in the case of the corresponding sinograms. This kind of lack of three dimensional information is not a problem in the case of the reconstructed images, since the three dimensional image (with cubic voxels) from the two dimensional cross–sections can be regarded as a truly three dimensional image. In the stackgram domain, the problem of the incomplete third dimension could be solved perhaps by using stackgrams generated from the planograms (that are extensions of the linograms (Eq. 2.5)). The planogram data enable truly three dimensional image reconstruction [8].

9.6 Extensions of Stackgram

In this thesis we have introduced the novel stackgram domain. The (three dimensional) stackgram is defined for parallel beam projections mapped by the two dimensional Radon transform. The stackgram approach or the idea of separating the signals along the trajectories could be advantageous also in different imaging geometries for processing of such data. Moreover, the stackgram domain approach is not restricted to be a mapping from the two dimensional sinograms.

The three different applications were employed for the new stackgram approach in the thesis. However, there might be also other applications for the stackgram concept in tomography. Ref. [9] suggests that an approach similar to the stackgram could be useful in image reconstruction, perhaps also in the case of three dimensional data (according to the article [9]).

Image reconstruction from the linograms (Eq. 2.5) does not require “explicit interpolation” at all [17], since the trajectories of the linogram data are straight lines (unlike the sinusoidal trajectories of the sinogram). Therefore, fast image reconstruction algorithms can be employed for the linogram data. A back–projection operator is also defined for the linograms. These suggest that the stackgram approach could be utilized also for the linogram data. Potential advantages, in contrast to the existing mapping from the sinogram to the stackgram, could be faster implementations, and besides, interpolation errors of the data could be (possibly) minimized due to the structure of the linograms.

In modern tomographs acquired data are three dimensional. Thus it would be useful to extend the definition of the stackgram domain for the three dimensional projection data. This would be especially beneficial for the reported alignment algorithm. As mentioned in Chapter 2, the X–ray transform and the Radon transform coincide in the two dimensional case [53]. The X–ray transform maps a three dimensional function, similarly as a two dimensional function, into a set of its line integrals. Therefore, the trajectories of the three dimensional X–ray transform could be separated in a similar manner as in the two dimensional case. Thus the X–ray transform may offer a potential way to extend the stackgrams for the three dimensional projection data. On the other hand, the higher dimensional linogram data, namely the (four dimensional) planograms [8], could provide a similar extension feasibility for the stackgrams. Ref. [15] considers a fast X–ray transform and it is mentioned that the planogram is "closely related" to the X–ray transform[2]. Since the planogram data are in use in modern PET tomographs, the planograms would provide a more preferable basis to extend the dimensionality of the stackgrams.

9.7 Concluding Remarks

We have proposed and tested a novel stackgram domain approach for tomographic data processing. The signals along the sinusoidal trajectories of the sinogram can be processed separately in the new stackgram domain. A reversible transformation from sinogram to stackgram employing the three–pass rotation algorithm with sinc–interpolation is introduced. According to our experiments, angular stackgram domain filtering seems to provide visually less disturbing noise structures in the reconstructed images, compared to commonly accepted radial sinogram domain filtering, although the resolution versus noise trade–off is advantageous for radial filtering. As regards to our filtering and extrapolation experiments, the angular information in the stackgram domain, unlike in the sinogram domain, can be exploited without introducing non–uniform or tangential blurring to the reconstructed images. An algorithm suitable for alignment of PET data using stackgrams has been introduced as well. The algorithm is simple, automatic, and it can align "locally rigid" transformations of the data. In general, in presence of noise, the performance of extrapolation and alignment in the stackgram domain could be improved by filtering of the stackgram data prior to further processing.

This thesis tests and mainly compares the unique stackgram approach with

[2]In Ref. [15], it is said that the term "slant stack" is equal to the linogram. In contrast, Ref. [7] claims that the slant stack coincides with the sinogram.

the sinogram based approaches. Accurate or advantageous results for practical applications still need to be studied more thoroughly. However, the results suggest that the stackgram approach can be applied successfully for filtering, extrapolation, and alignment of the tomographic data.

Bibliography

[1] S. Alenius and U. Ruotsalainen. Generalization of median root prior reconstruction. *IEEE Trans. Med. Imag.*, 21(11):1413–1420, November 2002.

[2] B. I. Andia, K. D. Sauer, and C. A. Bouman. Radially–dependent nonlinear sinogram filtering. In *Nuclear Science Symposium Conference Record*, volume 3, pages 1404–1408, October 2001.

[3] J. Astola and P. Kuosmanen. *Fundamentals of Nonlinear Digital Filtering*, pages 66–69. CRC Press, Boca Raton, New York, 1997.

[4] H. Baghaei, H. Li, J. Uribe, Y. Wang, and W. H. Wong. Compensation of missing projection data for MDAPET camera. In *Nuclear Science Symposium Conference Record*, volume 3, pages 17/41–17/45, October 2000.

[5] P. K. Banerjee and A. W. Toga. Image alignment by integrated rotational and translational transformation matrix. *Physics in Medicine and Biology*, 39:1969–1988, 1994.

[6] P. J. Besl and N. D. McKay. A method for registration of 3-D shapes. *IEEE Trans. Pattern Anal. Machine Intell.*, 14(2):239–256, February 1992.

[7] G. Beylkin. Discrete Radon transform. *IEEE Trans. Acoust., Speech, Signal Processing*, 35(2):162–172, February 1987.

[8] D. Brasse, P. E. Kinahan, R. Clackdoyle, M. Defrise, C. Comtat, and D. W. Townsend. Fast fully 3-D image reconstruction in PET using planograms. *IEEE Trans. Med. Imag.*, 23(4):413–425, 2004.

[9] F. J. Caramelo, N. C. Ferreira, L. Fazendeiro, and C. Souto. Image reconstruction by sinogram decomposition into sinusoidal curves. In *Proceedings of the 8th International Meeting on Fully Three–dimensional Image Reconstruction in Radiology and Nuclear Medicine*, pages 55–59, Salt Lake City, Utah, USA, July 2005.

[10] A. Chatziioannou and M. Dahlbom. Detailed investigation of transmission and emission data smoothing protocols and their effects on emission images. *IEEE Trans. Nucl. Sci.*, 43(1):290–294, February 1996.

[11] J. J. Clark, M. R. Palmer, and P. D Lawrence. A transformation method for the reconstruction of functions from nonuniformly spaced samples. *IEEE Trans. Acoust., Speech, Signal Processing*, 33(4):1151–1165, October 1985.

[12] A. M. Cormack. Sampling the Radon transform with beams of finite width. *Phys. Med. Biol.*, 23(6):11, 1978.

[13] M. E. Daube-Witherspoon and R. E. Carson. Investigation of angular smoothing of PET data. *IEEE Trans. Nucl. Sci.*, 44(6):2494–2499, December 1997.

[14] A. H. Delaney and Y. Bresler. A fast and accurate Fourier algorithm for iterative parallel–beam tomography. *IEEE Trans. Image Processing*, 5(5):740–753, May 1996.

[15] D. L. Donoho and O. Levi. Fast X–ray and beamlet transforms for three–dimensional data. *Modern Signal Processing, MSRI Publications*, 46:79–116, 2003.

[16] S. R. Dooley and A. K. Nandi. Notes on the interpolation of discrete periodic signals using sinc function related approaches. *IEEE Trans. Signal Processing*, 48(4):1201–1203, April 2000.

[17] P. R. Edholm, G. T. Herman, and D. A. Roberts. Image reconstruction from linograms: Implementation and evaluation. *IEEE Trans. Med. Imag.*, 7(3):239–246, 1988.

[18] J. M. Fitzpatrick, J. B. West, and C. R. Maurer. Predicting error in rigid-body point-based registration. *IEEE Trans. Med. Imag.*, 17(5):694–702, October 1998.

[19] R. Freifelder, C. Cardi, I. Grigoras, J. R. Saffer, and J. S. Karp. First results of a dedicated breast PET imager, BPET, using NaI(Tl) curve plate detectors. In *IEEE Nuclear Science Symposium Conference Record, 2001*, pages 1241–1245, San Diego, CA, 2001.

[20] R. C. Gonzales and R. E. Woods. *Digital Image Processing*, pages 112, 118. Addison–Wesley, USA, 1992.

[21] A. Gotchev, K. Egiazarian, and T. Saramäki. Comparing the performance of optimized piece-wise polynomial image interpolators. In *Proceedings of the 5th Nordic Signal Processing Symposium*, page 5 pages, Norway, October 2002.

[22] P. J. Green. Bayesian reconstructions from emission tomography data using a modified EM algorithm. *IEEE Trans. Med. Imag.*, 9(1):84–93, March 1990.

[23] G. T. Herman. *Image Reconstruction from Projections: Implementations and Applications*, pages 1–80. Springer–Verlag, Berlin Heidelberg New York, 1979.

[24] G. T. Herman. *Image Reconstruction from Projections: The Fundamentals of Computerized Tomography*, pages 1–38, 108–117. Academic Press, New York, NY, 1980.

[25] D. L. G. Hill, P. G. Batchelor, M. Holden, and D. J. Hawkes. Medical image registration. *Physics in Medicine and Biology*, 46:R1–R45, 2001.

[26] B. F. Hutton, A. Z. Kyme, Y. H. Lau, D. W. Skerret, and R. R. Fulton. A hybrid 3–D reconstruction/registration algorithm for correction of head motion in emission tomography. *IEEE Trans. Nucl. Sci.*, 49(1):188–194, February 2002.

[27] E. C. Ifeachor and B. W. Jervis. *Digital Signal Processing: A Practical Approach*, pages 278–373. Addison-Wesley, USA, 1996.

[28] J. S. Jaffe. Limited angle reconstruction using stabilized algorithms. *IEEE Trans. Med. Imag.*, 9(3):338–344, September 1990.

[29] A. Jain. *Fundamentals of Digital Image Processing*, pages 434–448. Prentice-Hall International, Englewood Cliffs, NJ, 1989.

[30] A. K. Jain and S. Ranganath. Extrapolation algorithms for discrete signals with application in spectral estimation. *IEEE Trans. Acoust., Speech, Signal Processing*, 29(4):830–845, August 1981.

[31] J. P. Kaipio and E. Somersalo. *Statistical and Computational Inverse Problems*, pages 49–100. Springer-Verlag, 2004.

[32] A. K. Kak and M. Slaney. *Principles of Computerized Tomographic Imaging*, pages 49–112. IEEE Press, New York, NY, 1988.

[33] C.-M. Kao, M. N. Wernick, and C-T. Chen. Kalman sinogram restoration for fast and accurate PET image reconstruction. *IEEE Trans. Nucl. Sci.*, 45(6):3022–3029, December 1998.

[34] J. S. Karp, G. Muehllehner, and R. M. Lewitt. Constrained Fourier space method for compensation of missing data in emission computed tomography. *IEEE Trans. Med. Imag.*, 7(1):21–25, March 1988.

[35] J.S. Karp, G. Muehllehner, D.A. Mankoff, C.E. Ordonez, J.M. Ollinger, M.E. Daube-Witherspoon, A.T. Haigh, and D.J. Beerbohm. Continuous-slice PENN-PET: a positron tomograph with volume imaging capability. *Journal of Nuclear Medicine*, 31(5):617–627, 1990.

[36] I. G. Kazantsev, R. Van de Walle, and I. Lemahieu. Ridge functions, natural pixels and minimal norm reconstruction. *IEEE Trans. Nucl. Sci.*, 47(3):1118–1122, June 2000.

[37] I. G. Kazantsev, S. Matej, and R. M. Lewitt. Limited angle tomography and ridge functions. In *IEEE Nuclear Science Symposium Conference Record*, pages 1706–1710, November 2002.

[38] P. E. Kinahan, F. Fessler, and J. S. Karp. Statistical image reconstruction in PET with compensation for missing data. *IEEE Trans. Nucl. Sci.*, 44(4):1552–1557, August 1997.

[39] D. Kincaid and W. Cheney. *Numerical Analysis – Second Edition*, pages 330–489. Brooks/Cole Publishing Company, Pacific Grove CA, 1996.

[40] A. E. Kostopoulos, A. P. Happonen, and U. Ruotsalainen. Three-dimensional alignment of objects in dynamic pet scans using filtered sinusoidal trajectories of sinogram. In *3rd International Conference on Imaging Technologies in Biomedical Sciences*, Milos Island, Greece, September 2005 (to appear).

[41] E. Krestyannikov, A. Happonen, and U. Ruotsalainen. Noise models for sinusoidal trajectories composing sinogram data in positron emission tomography. In *Proceedings of the 6th Nordic Signal Processing Symposium*, pages 77–80, Helsinki, Finland, 2004.

[42] K. Lange and R. Carson. EM reconstruction algorithms for emission and transmission tomography. *Journal of Computer Assisted Tomography*, 8(2):306–316, 1984.

[43] R. M. Lewitt. Reconstruction algorithms: Transform methods. *Proceedings of the IEEE*, 71(3):390–408, March 1983.

[44] X. Li, H. Lu, G. Han, and Z. Liang. A noise reduction method for non–stationary noise model of SPECT sinogram based on kalman filter. In *Nuclear Science Symposium Conference Record*, volume 4, pages 2134–2138, October 2001.

[45] A. K. Louis. Incomplete data problems in X-ray computerized tomography. *Numerische Mathematik*, 48:251–262, 1986.

[46] W. Lu and T. R. Mackie. Tomographic motion detection and correction directly in the sinogram space. *Physics in Medicine and Biology*, 47:1267–1284, 2002.

[47] F. Maes, A. Collignon, D. Vandermeulen, G. Marchal, and P. Suetens. Multimodality image registration by maximization of mutual information. *IEEE Trans. Med. Imag.*, 16(2):187–198, April 1997.

[48] J. B. A. Mainz, P. van den Elsen, and M. A. Viergever. Evaluation of ridge seeking operators for multimodality medical image matching. *IEEE Trans. Pattern Anal. Machine Intell.*, 18(4):353–365, April 1996.

[49] J. B. A. Mainz and M. A. Viergever. A survey of medical image registration. *Medical Image Analysis*, 2(1):1–36, 1998.

[50] I. Maravic and M. Vetterli. A sampling theorem for the Radon transform of finite complexity objects. In *Proceedings of the IEEE International Conference on Acoustics, Speech, and Signal Processing*, volume 2, pages 1197–1200, 2002.

[51] P. Milanfar. A model of the effect of image motion in the Radon transform. *IEEE Trans. Image Processing*, 8(9):1276–1281, September 1999.

[52] J. Modersitzki. *Numerical Methods for Image Registration*, pages 14–23, 71–74, 77–82. Oxford University Press, New York, NY, 2004.

[53] F. Natterer. *The Mathemathics of Computerized Tomography*, pages 1–84, 103–179. John Wileys and Sons, B. G. Teubner, 1986.

[54] J Nuyts, C Michel, and P Dupont. Maximum-likelihood expectation-maximization reconstruction of sinograms with arbitrary noise distribution using NEC-transformations. *IEEE Trans. Med. Imag.*, 20(5):365–375, October 2001.

[55] J. M. Ollinger and J. A. Fessler. Positron-emission tomography. *IEEE Signal Processing Mag.*, 14(1):43–55, 1997.

[56] J. M. Ollinger and J. S. Karp. An evaluation of three algorithms for reconstructing images from data with missing projections. *IEEE Trans. Nucl. Sci.*, 35(1):629–634, February 1988.

[57] T. Olson. Stabilized inversion for limited angle tomography: A tutorial overview. *IEEE Eng. Med. Biol. Mag.*, 14(5):612–620, September 1995.

[58] T. Olson and J. S. Jaffe. An explanation of the effects of squashing in limited angle tomography. *IEEE Trans. Med. Imag.*, 9(3):242–246, September 1990.

[59] P. Oskoui and H. Stark. A comparative study of three reconstruction methods for a limited-view computer tomography problem. *IEEE Trans. Med. Imag.*, 8(1):43–49, March 1989.

[60] X. Pan. Quasi–bandlimited properties of Radon transforms and their implications for increasing angular sampling densities. *IEEE Trans. Med. Imag.*, 17(3):395–406, 1998.

[61] A. Papoulis. A new algorithm in spectral analysis and band–limited extrapolation. *IEEE Trans. Circuits Syst.*, 22(9):735–742, September 1975.

[62] M. Pedersen. *Functional Analysis in Applied Mathematics and Engineering*, pages 1–23. Chapman and Hall/CRC, USA, 2000.

[63] C. A. Pelizzari, G. T. Chen, D. R. Spelbring, R. R. Weichselbaum, and C. T. Chen. Accurate three-dimensional registration of CT, PET, and/or MR images of the brain. *J. Comput. Assist. Tomogr.*, 13(1):20–26, January 1989.

[64] Y. Picard and C. J. Thompson. Motion correction of PET images using multiple acquisition frames. *IEEE Trans. Med. Imag.*, 16(2):137–144, April 1997.

[65] V. Potesil. Respiratory motion compensation in the stackgram domain for lung PET imaging. Master's thesis, Brno University of Technology, Faculty of Electrical Engineering and Communication/Tampere University of Technology, Department of Information Technology, 2005. Supervisors: U. Ruotsalainen and A. P. Happonen.

[66] P. A. Rattey and A. G. Lindgren. Sampling the 2-D Radon transform. *IEEE Trans. Acoust., Speech, Signal Processing*, 29(5):994–1002, October 1981.

[67] J. A. Reeds and L. A. Shepp. Limited angle reconstruction in tomography via squashing. *IEEE Trans. Med. Imag.*, 6(2):89–97, June 1987.

[68] P. J. La Riviere and X. Pan. Nonparametric regression sinogram smoothing using a roughness-penalized poisson likelihood objective function. *IEEE Trans. Med. Imag.*, 19(8):773–786, August 2000.

[69] T. Rohlfing, D. B. Russakoff, and C. R. Maurer. Performance-based classifier combination in atlas-based image segmentation using expectation-maximization parameter estimation. *IEEE Trans. Med. Imag.*, 23(8):983–994, August 2004.

[70] M. S. Sabri and W. Steenaart. An approach to band–limited signal extrapolation: The extrapolation matrix. *IEEE Trans. Circuits Syst.*, 25(2):74–78, February 1978.

[71] B. G. Salomon and H. Ur. Accelerated iterative band–limited extrapolation algorithms. *IEEE Signal Processing Letters*, 11(11):871–874, November 2004.

[72] M. I. Sezan and H. Stark. Image restoration in CT by the method of projections onto convex sets. In *IEEE International Conference on Acoustics, Speech, and Signal Processing*, volume 8, pages 139 – 142, Boston, USA, 1983.

[73] S. Siltanen, V. Kolehmainen, S. Järvenpää, J. P. Kaipio, P. Koistinen, M. Lassas, J. Pirttilä, and E. Somersalo. Statistical inversion for medical X-ray tomography with few radiographs: I. general theory. *Physics in Medicine and Biology*, 48:1437–1463, 2003.

[74] C. W. Stearns. Context–sensitive angular filtering of PET transmission data. In *Nuclear Science Symposium and Medical Imaging Conference Record*, volume 3, pages 1332–1334, October 1994.

[75] P. Thevenaz, T. Blu, and M. Unser. Interpolation revisited. *IEEE Trans. Med. Imag.*, 19(7):739–758, July 2000.

[76] K. Thielemans and S. Mustafovic. Image reconstruction of motion corrected sinograms. In *Nuclear Science Symposium Conference Record*, volume 4, pages 2401–2406, October 2004.

[77] J. P. Thirion. Non–rigid matching using demons. In *Proceedings of Computer Vision and Pattern Recognition*, pages 245–251, June 1996.

[78] J. Tohka and J. Mykkänen. Deformable mesh for automated surface extraction from noisy images. *International Journal of Image and Graphics, Special Issue on Deformable Models for Image Analysis and Pattern Recognition*, 4(3):405–432, July 2004.

[79] H. Treuer, S. Hunsche, M. Hoevels, K. Luyken, M. Maarouf, J. Voges, and V. Sturm. The influence of head frame distortions on stereotactic localization and targeting. *Physics in Medicine and Biology*, 49:3877–3887, 2004.

[80] M. Unser, P. Thevenaz, C. Lee, and U. E. Ruttimann. Registration and statistical analysis of PET images using the wavelet transform. *IEEE Eng. Med. Biol. Mag.*, 14(5):603–611, September 1995.

[81] M. Unser, P. Thevenaz, and L. Yaroslavsky. Convolution–based interpolation for fast, high quality rotation of images. *IEEE Trans. Image Processing*, 4(10):1371–1381, October 1995.

[82] P. A. van den Elsen, E.-J. D. Pol, and M. A. Viergever. Medical image matching – a review with classification. *IEEE Eng. Med. Biol. Mag.*, 12(1):26–39, 1993.

[83] S. K. Woo, H. Watabe, Y. Choi, K. M. Kim, C. C. Park, P. M. Bloomfield, and H. Iida. Sinogram-based motion correction of PET images using optical motion tracking system and list-mode data acquisition. *IEEE Trans. Nucl. Sci.*, 51(3):782–788, June 2004.

[84] R. P. Woods, S. R. Cherry, and J. C Mazziotta. Rapid automated algorithm for aligning and reslicing PET images. *Journal of Computer Assisted Tomography*, 16:620–633, 1992.

[85] X.-L. Xu, J.-S. Liow, and S. C. Strother. Iterative algebraic reconstruction algorithms for emission computed tomography: A unified framework and its applications to positron emission tomography. *Med. Phys.*, 20(6):1675–1684, November 1993.

[86] L. Yaroslavsky. Efficient algorithm for discrete sinc interpolation. *Applied Optics*, 36(2):460–463, January 1997.

[87] L. Yaroslavsky. Boundary effect free and adaptive discrete signal sinc–interpolation algorithms for signal and image resampling. *Applied Optics – IP*, 42(20):4166–4175, July 2003.

[88] L. Yaroslavsky, A. Happonen, and Y. Katiyi. Discrete signal sinc-interpolation in DCT domain: Fast algorithms. In *Proceedings of International TICSP Workshop on Spectral Methods and Multirate Signal Processing*, pages 179–185, Toulouse, France, September 2002.

[89] L. P. Yaroslavsky and Y. Chernobrodov. DFT and DCT based discrete sinc-interpolation methods for direct Fourier tomographic reconstruction. In *Proceedings of the 3rd International Image and Signal Processing and Analysis*, volume 1, pages 405–410, September 2003.

[90] Sze Fong Yau and Shum Him Wong. A linear sinogram extrapolator for limited angle tomography. In *3rd International Conference on Signal Processing*, pages 386–389, Beijing, China, October 1996.

[91] D.-C. Yu and S.-C. Huang. Study of reprojection methods in terms of their resolution loss and sampling errors. *IEEE Trans. Nucl. Sci.*, 40(4):1174–1178, August 1993.

Publications

Publication 1

A. P. Happonen and S. Alenius
"Sinogram Filtering Using a Stackgram Domain"
Proceedings of the Second IASTED International Conference: Visualization, Imaging and Image Processing
Malaga, Spain, September 9-12, 2002, pp. 339-343

Publication 2

A. P. Happonen and S. Alenius
”Investigation of Sinogram Filtering Using Stackgram Domain”
IEEE Transactions on Medical Imaging
(submitted, February 2003)
Published as a technical report of Tampere University of Technology,
Institute of Signal Processing, *Report 2005:1*, October 2005

Publication 3

A. P. Happonen and S. Alenius
“A Comparison of Sinogram and Stackgram Domain Filtering Methods Employing L-Filters for Noise Reduction of Tomographic Data”
Proceedings of the 2005 Finnish Signal Processing Symposium
Kuopio, Finland, August 25, 2005, pp. 1-4

Publication 4

A. P. Happonen and U. Ruotsalainen
"A Comparative Study of Angular Extrapolation in Sinogram and Stackgram Domains for Limited Angle Tomography"
14th Scandinavian Conference SCIA 2005, Lecture Notes in Computer Science
Vol. 3540, June 2005, pp. 1047-1056

Publication 5

A. P . Happonen and U. Ruotsalainen
”Three-Dimensional Alignment of Scans in a Dynamic PET Study Using Sinusoidal Trajectory Signals of a Sinogram”
IEEE Transactions on Nuclear Science
Vol. 51, No. 5, October 2004, pp. 2620-2627

Tampereen teknillinen yliopisto
PL 527
33101 Tampere

Tampere University of Technology
P.O. Box 527
FIN-33101 Tampere, Finland